The Astrophysical Journal, 754:3 (18pp), 2012 July 20 doi:10.1088/0004-637X/754/1/3

DEEP ABSORPTION LINE STUDIES OF QUIESCENT GALAXIES AT $z \sim 2$: THE DYNAMICAL-MASS–SIZE RELATION AND FIRST CONSTRAINTS ON THE FUNDAMENTAL PLANE*

S. Toft[1], A. Gallazzi[1], A. Zirm[1], M. Wold[1], S. Zibetti[1,2], C. Grillo[1], and A. Man[1]
[1] Dark Cosmology Centre, Niels Bohr Institute, University of Copenhagen, Juliane Mariesvej 30, DK-2100 Copenhagen, Denmark; sune@dark-cosmology.dk
[2] INAF-Osservatorio Astrofisico di Arcetri, Largo Enrico Fermi 5, I-50125 Firenze, Italy

Received 2011 December 30; accepted 2012 April 23; published 2012 June 27

ABSTRACT

We present dynamical and structural scaling relations of quiescent galaxies at $z = 2$, including the dynamical-mass–size relation and the first constraints on the fundamental plane (FP). The backbone of the analysis is a new, very deep Very Large Telescope/X-shooter spectrum of a massive, compact, quiescent galaxy at $z = 2.0389$. We detect the continuum between 3700 and 22,000 Å and several strong absorption features (Balmer series, Ca H+K, G band) from which we derive a stellar velocity dispersion of 318 ± 53 km s^{-1}. We perform detailed modeling of the continuum emission and line indices and derive strong simultaneous constraints on the age, metallicity, and stellar mass. The galaxy is a dusty ($A_V = 0.77^{+0.36}_{-0.32}$) solar metallicity ($\log(Z/Z_\odot) = 0.02^{+0.20}_{-0.41}$) post-starburst galaxy, with a mean-luminosity-weighted log(age/yr) of 8.9 ± 0.1. The galaxy formed the majority of its stars at $z > 3$ and currently has little or no ongoing star formation. We compile a sample of three other $z \sim 2$ quiescent galaxies with measured velocity dispersions, two of which are also post-starburst like. Their dynamical-mass–size relation is offset significantly less than the stellar-mass–size relation from the local early-type relations, which we attribute to a lower central dark matter fraction. Recent cosmological merger simulations agree qualitatively with the data, but cannot fully account for the evolution in the dark matter fraction. The $z \sim 2$ FP requires additional evolution beyond passive stellar aging to be in agreement with the local FP. The structural evolution predicted by the cosmological simulations is insufficient, suggesting that additional, possibly non-homologous, structural evolution is needed.

Key words: cosmology: observations – galaxies: distances and redshifts – galaxies: elliptical and lenticular, cD – galaxies: evolution – galaxies: formation – galaxies: stellar content

Online-only material: color figures

1. INTRODUCTION

Since first being discovered in NIR surveys (e.g., FIRES; Franx et al. 2003), massive, evolved galaxies at $z \sim 2$ have been a subject of extensive research, characterizing their properties from increasingly larger and more complete samples (e.g., van Dokkum et al. 2006; Franx et al. 2008; Toft et al. 2009; McCracken et al. 2010; Williams et al. 2010; Newman et al. 2011; Damjanov et al. 2011; Cassata et al. 2011; Wuyts et al. 2011). By combining photometric redshifts, stellar masses, and star formation histories (SFHs) derived from spectral energy distribution (SED) fits to broadband photometry investigators have probed their general properties: they are massive ($M > 10^{11}\,M_\odot$) galaxies, with space densities $\sim 5 \times 10^{-4}$ Mpc^{-3} (van Dokkum et al. 2010; Marchesini et al. 2009) which cluster strongly (Daddi et al. 2003; Quadri et al. 2008) and approximately 30%–50% of them are quiescent, with little or no star formation (e.g., Kriek et al. 2006, 2009; Toft et al. 2007, 2009). In high-resolution imaging, the star-forming galaxies have extended and in some cases disturbed morphologies, while most quiescent galaxies are extremely compact (effective radius $r_e \lesssim 1$ kpc), corresponding to average stellar mass densities (within r_e) 1–2 orders of magnitude higher than in local early types (Daddi et al. 2005; Toft et al. 2005, 2007; Trujillo et al. 2006; Zirm et al. 2007; Cimatti et al. 2008; Kriek et al. 2009; Conselice et al. 2011; Cassata et al. 2011; Wuyts et al. 2011), but see also Mancini et al. (2010) and Newman et al. (2010). Furthermore, there is evidence that a significant fraction of $z \sim 2$ quiescent galaxies have flat, exponential-disk-like surface brightness profiles, rather than the $r^{1/4}$ profiles found in local quiescent galaxies (Toft et al. 2005, 2007; van Dokkum et al. 2008; van der Wel et al. 2011; Wuyts et al. 2011).

Galaxies with these properties are extremely rare in the local universe, and the ones that have been identified have similar ages as their $z \sim 2$ counterparts, and can thus not be their descendents (Trujillo et al. 2009; Taylor et al. 2010; Shih & Stockton 2011; Ferré-Mateu et al. 2012). The evolutionary path of the compact quiescent galaxies to the local universe is not well understood. Their high stellar masses, compact morphologies, and quiescent nature make it natural to assume they are the progenitors, or "seeds" of massive local early-type galaxies, which is also supported by number density arguments (van Dokkum et al. 2010), but they have to go through significant structural evolution, increasing their effective radii by factors of 3–6, and possibly transforming their flat exponential-disk-like structure into bulge-dominated/early-type systems. In the following, we will refer to these massive quiescent compact $z \sim 2$ galaxies as SEEDs. Minor and major dry merging are the primary candidate processes for puffing up their sizes and transforming their profiles from flat disk-like systems to spheroidal early types (e.g., Khochfar & Silk 2006; Naab et al. 2009; Bezanson et al. 2009).

One of the main uncertainties in the interpretation of the properties of SEEDs is that it is mainly based on photometric redshifts and SED fits to broadband photometry. Due to their quiescence, they are void of strong emission lines and have very faint rest-frame ultraviolet (UV) continua. It is challenging to detect absorption lines that can be used for redshift determination of quiescent systems. The red rest-frame optical color

---

* Based on X-shooter–VLT observations collected at the European Southern Observatory, Paranal, Chile (program IDs 084.A-0303, 084.A-035A).

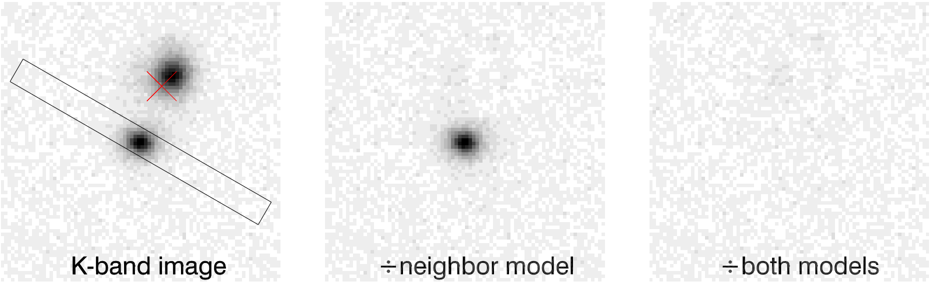

Figure 1. Left: *K*-band image (10.″7 × 10.″7) of UDS19627 (WFCAM), with the position of the X-shooter 11″ × 0.″9 slit indicated. North is up, east is to the left. The seeing is 0.″7. The brighter galaxy northwest of the target is at lower redshift. Middle: we modeled the surface brightness profiles of the two galaxies simultaneously with GALFIT. In this image the best-fitting model of the neighbor has been subtracted, demonstrating its minimal influence on our fit of the main target. Right: residual after subtracting both best-fitting surface brightness models. The red cross indicates the centroid of a 24 μm source associated with the foreground galaxy.

(A color version of this figure is available in the online journal.)

Table 1
Photometry: AB Magnitudes for UDS19627 from the UDS Survey (Williams et al. 2010)

U	*B*	*V*	*R*	*I*	*z*	*J*	*H*	*K*	Ch1	Ch2
25.72 ±0.21	24.76 ±0.03	23.94 ±0.03	23.47 ±0.03	23.15 ±0.03	22.62 ±0.03	20.94 ±0.03	20.46 ±0.03	20.19 ±0.02	19.67 ±0.03	19.58 ±0.04

Note. Ch1 and Ch2 refer to *Spitzer*/IRAC 3.6 and 4.5 μm bands.

of SEEDs makes them brighter in the observed near-infrared (NIR), but due to the limited sensitivity of NIR spectrographs, spectroscopic confirmations have only been possible for small samples of the very brightest examples. In an NIR spectroscopic survey of nine of the brightest examples, using the Gemini Near Infrared Spectrograph (GNIRS), Kriek et al. (2006) were able to detect the continuum well enough to determine the redshift from the position of the 4000 Å break, and confirm the relatively old age (1–2 Gyr) and quiescence from the shape of the continuum and lack of strong emission lines. Even with relatively long exposure times (1–4 hr) on an 8 m telescope it was not possible to make significant detections of absorption lines. Only in a much deeper (29 hr) follow-up spectrum were absorption lines detected for one object (Kriek et al. 2009). In this case, it was also possible to measure the stellar velocity dispersion of a $z \sim 2$ galaxy for the first time. The dispersion is very high, consistent with what was expected from its high derived stellar mass density (Toft et al. 2007; Cimatti et al. 2008; van Dokkum et al. 2009). Since then velocity dispersions have been derived for a few handfuls of quiescent galaxies in the redshift range $1 < z < 2$ (Cenarro & Trujillo 2009; Cappellari et al. 2009; Newman et al. 2010; Onodera et al. 2010; van de Sande et al. 2011).

With the advent of new, more sensitive spectrographs it is now feasible to obtain "absorption line quality" spectra for samples of SEED galaxies in reasonable amounts of time. In this paper, we present the first results of such a survey that we conducted with the X-shooter spectrograph on the Very Large Telescope (VLT). As this is the first detailed spectroscopic investigation of this type of galaxy, we describe stellar population and velocity dispersion fits in considerable detail.

The structure of the paper is as follows. In Section 2 we describe the target selection, acquisition, and reduction of a deep X-shooter spectrum of a quiescent galaxy at $z \sim 2$. In Sections 3 and 4 we perform a detailed analysis of the spectrum, fitting the UV–NIR continuum and absorption line indices, with stellar population synthesis models, to derive stringent constraints on the age, stellar mass, dust content, and metallicity of the galaxy. In Section 5, we fit the surface brightness profile of the galaxy to derive its structural parameters. In Section 6 we measure the velocity dispersion from the absorption lines, and derive the dynamical mass. In Section 7 we compile a sample of three other $z \sim 2$ galaxies from the literature with measured velocity dispersions, and compare scaling relations between their structural and dynamical properties with those observed in local galaxies, to derive constraints on the dynamical-mass–size relation and, for the first time, the fundamental plane (FP) relations at $z = 2$. Finally, we summarize and discuss the results in Section 8. Throughout the paper, we assume a standard flat cosmology $(\Omega_\Lambda, \Omega_M = (0.7, 0.3)$, $H_0 = 73$ km s^{-1} Mpc^{-1}). All magnitudes are referenced to the AB system (Oke 1974).

2. OBSERVATIONS

2.1. *Target Selection*

Our objective was to take advantage of the unique combination of sensitivity, spectral coverage, and resolution of X-shooter to obtain a spectrum of a SEED galaxy of unprecedented quality, to allow a detailed study of the absorption lines for the first time, and to obtain a spectrum of sufficient signal to noise (S/N) to be used as a template for designing programs to observe larger samples.

The target UDS19627 (R.A. = 02:18:17.1, decl. = −05:21:38.8) was chosen from the UKIRT Ultra Deep Survey (UDS), as a (*K* band) bright example of a compact, quiescent, massive galaxy with $z \sim 2$ (Williams et al. 2010). Based on the broadband photometry (see Table 1), the target is a very massive, quiescent galaxy at $z_{\mathrm{phot}} = 2.02^{+0.07}_{-0.08}$ with $K = 20.19 \pm 0.01$. Images of the target are shown in Figure 1. The bright galaxy $\sim$3″ northwest of the target is at lower redshift (UDS19771, $z_{\mathrm{phot}} = 0.58$; Williams et al. 2010). This galaxy may be boosting the brightness of our target slightly, through the gravitational lensing effect (see Section 7.8).

2.2. *X-shooter Data*

We obtained deep spectra with the X-shooter spectrograph mounted on ESO's VLT. X-shooter is a single-object echelle

Table 2
Details of the X-shooter Observations

Night	Exptime (s) [UVB/OPT/NIR]	Slit Size ($''$) [UVB/OPT/NIR]
2010 Oct 19	4 × 800/4 × 800/4 × 900	0.8 × 11/0.9 × 11/0.6 × 11
2010 Oct 20	8 × 800/8 × 800/8 × 900	1.0 × 11/0.9 × 11/0.9 × 11
2010 Oct 21	8 × 800/8 × 800/8 × 900	1.0 × 11/0.9 × 11/0.9 × 11

spectrograph, consisting of three arms which cover simultaneously the spectral range 3000–25,000 Å (Vernet et al. 2011). We obtained a total exposure time of 5 hr over three nights from 2009 October 19 to 21 as part of the X-shooter GTO program. Details of the observations are given in Table 2. On the first night the seeing was very good (FWHM$\sim0\farcs5$), so we used a narrow slit. On the following nights the seeing was $0\farcs7 - 1\farcs0$, so we switched to a larger slit width to minimize slit loss. We performed a blind offset to the object from a nearby bright star, and nodded on the slit with an ABA′B′ sequence with four independent positions.

2.3. *Reduction*

We reduced the data using a combination of the ESO X-shooter pipeline (version 1.2.0 in physical mode) and our own scripts. We experimented with different reduction recipes.

The cleanest, highest S/N spectrum (between the skylines) was achieved when reducing the individual exposures in STARE mode. To determine accurate offset between the trace in different exposures, we "collapsed" regions between skylines in the rectified, sky-subtracted frames and measured the shifts between the peaks of the spectral point-spread functions (SPSF; the object is effectively a point source due to the seeing). We then shifted the individual exposures to the same position and combined them by computing the sigma clipped average of each pixel (masking out bad pixels and cosmic rays). We also created a two-dimensional variance map in which each pixel is the variance of the 20 pixels in the stack.

The individual background-subtracted, rectified two-dimensional NIR frames were corrected for telluric absorption, using telluric star observations that were observed immediately before or after each 1 hr observation block.

This correction was then applied to each row in the individual two-dimensional frames before they were combined. Finally, we extracted the one-dimensional spectrum, using optimal extraction (Horne 1986), weighting the pixels both by the SPSF and by their variance. For flux calibration, we used a spectrum of the spectrophotometric standard BD +17°C4708 (Bohlin & Gilliland 2004) in combination with the CALSPEC *Hubble Space Telescope* (*HST*) database (Bohlin 2007). To correct for slit losses we compared to the broadband photometry, and applied a constant scaling to each of the three arms.

3. SPECTRAL ANALYSIS

In Figure 2 we show the full composite 3500–20,000 Å X-shooter spectrum, constructed by stitching together the flux-calibrated UVB, VIS, and NIR arm spectra. The spectrum confirms the expectation from the broadband photometry that the galaxy is a massive quiescent galaxy at $z\sim2$, with a strong 4000 Å break in the J band. Interestingly, the (flat) rest-frame UV continuum of the galaxy is detected throughout the VIS and UVB arms, all the way down to ∼3700 Å. The overall shape of the continuum is characteristic of a post-starburst or E+A galaxy (e.g., Quintero et al. 2004) rather than of an early-type galaxy. A number of strong absorption lines are detected (Balmer series, Ca H+K, G band). From the absorption lines we derive a redshift of 2.0389 ± 0.0004.

4. STELLAR POPULATION PROPERTIES

In order to constrain the galaxy stellar populations, we analyze the X-shooter spectrum by means of a Monte Carlo library of 100,000 model spectra, based on Bruzual & Charlot (2003, hereafter BC03) simple stellar population (SSP) models convolved with random SFHs. We adopt a Chabrier (2003) initial mass function (IMF). The SFHs are modeled with an exponentially declining function on top of which random bursts of star formation can occur. Following Charlot & Fall (2000), attenuation by dust is modeled by means of the total effective optical depth τ_V experienced by young ($<10^7$ yr) stars still in their birth cloud and the fraction μ of it contributed by the ISM.[3]

We adopt a Bayesian statistical approach in which all models in the library are compared to the observed galaxy. The likelihood of each model is computed as $\exp(-\chi^2/2)$ by comparing a selected set of observables with the model predictions. The posterior probability density function (PDF) of each physical parameter of interest is computed by weighting all the models by their likelihood and marginalizing over all the other parameters (see, e.g., Kauffmann et al. 2003; Gallazzi et al. 2005; Salim et al. 2005). The estimated parameter is taken from the median of the corresponding PDF, while the confidence interval is estimated from the 16th and 84th percentiles of the PDF. In particular we derived PDFs of the luminosity- and mass-weighted ages, the stellar metallicity, the stellar mass, and the parameters describing dust attenuation.

In order to compare the data with the models, we use a lower resolution version of the X-shooter spectrum binned over 18 pixels[4] which corresponds to a rest-frame $\Delta\lambda = 3$ Å comparable to the spectral resolution of the BC03 models in the optical range. We adopt a larger $\Delta\lambda$ of 16 Å in the rest-frame UV (UVB and VIS arms) to match the lower resolution of the models in this regime. Finally, the observed spectrum is corrected for foreground Galactic reddening ($A_V = 0.0689$) adopting the extinction maps of Schlegel et al. (1998) and put in the rest frame. The model spectra are convolved with a range of velocity dispersions that account for the measured velocity dispersion and associated uncertainties (particularly relevant in the optical range and for absorption index measures).

In order to put constraints on the above mentioned parameters, we combine information from individual stellar absorption features (see Figure 3) with UV and optical colors. The indices

---

[3] We adopt the model library used in Salim et al. (2005), but we restrict the formation time to vary between the age of the universe at the redshift of the galaxy (i.e., 3.2 Gyr) and 1.5 Gyr in order to reproduce the current quiescent nature of the galaxy as witnessed by the lack of emission lines (we checked that the precise choice of minimum formation time does not affect the stellar mass estimates and only minimally the age estimates). The other parameters defining the SFH and dust attenuation follow the same prior distributions as in Salim et al. (2005). The star formation timescale can vary between 0 and 1 Gyr^{-1}. The probability of having a burst is set such that 50% of the models experience a burst in the last 2 Gyr. Bursts are parameterized in terms of the fraction of stellar mass produced, which is logarithmically distributed between 0.03 and 4, and their duration can vary between 3×10^7 and 3×10^8 yr. The metallicity of each model can vary between 10% and two times solar and it is fixed along the SFH. The total effective optical depth τ_V can vary between 0 and 6, and μ can vary between 0.1 and 1.

[4] The binned spectrum is computed as the noise-weighted median flux in each bin and the error is obtained from the noise-weighted 16th and 84th percentiles.

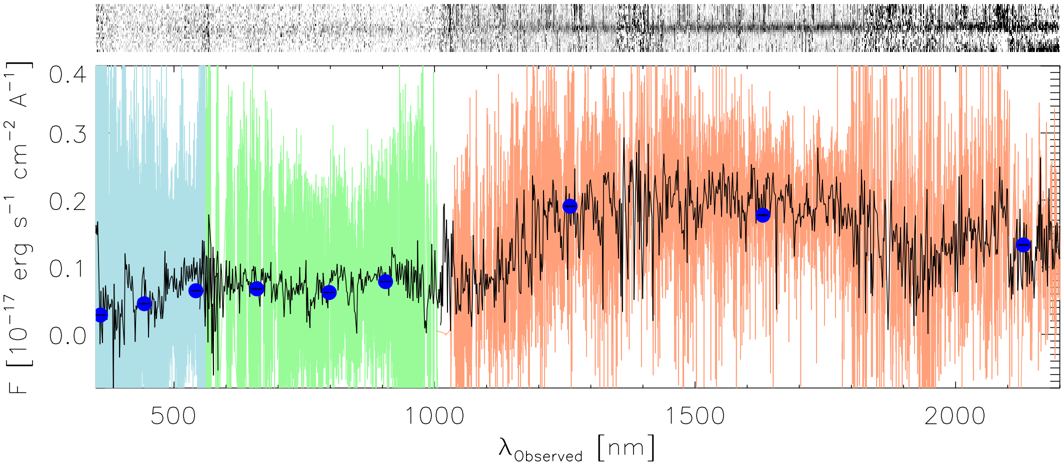

Figure 2. Full two-dimensional (top) and extracted one-dimensional (bottom) X-shooter UVB (blue), VIS (green), and NIR (red) spectrum of UDS19627 (corrected for slit losses). The colored curves show the full resolution (0.5 Å) spectrum, the black curve is binned to a resolution of 10 Å, where the value in each bin is the weighted median of the individual pixel values. Also plotted are the broadband fluxes (blue circles). A number of absorption lines are detected (see also Figures 9 and 10).

(A color version of this figure is available in the online journal.)

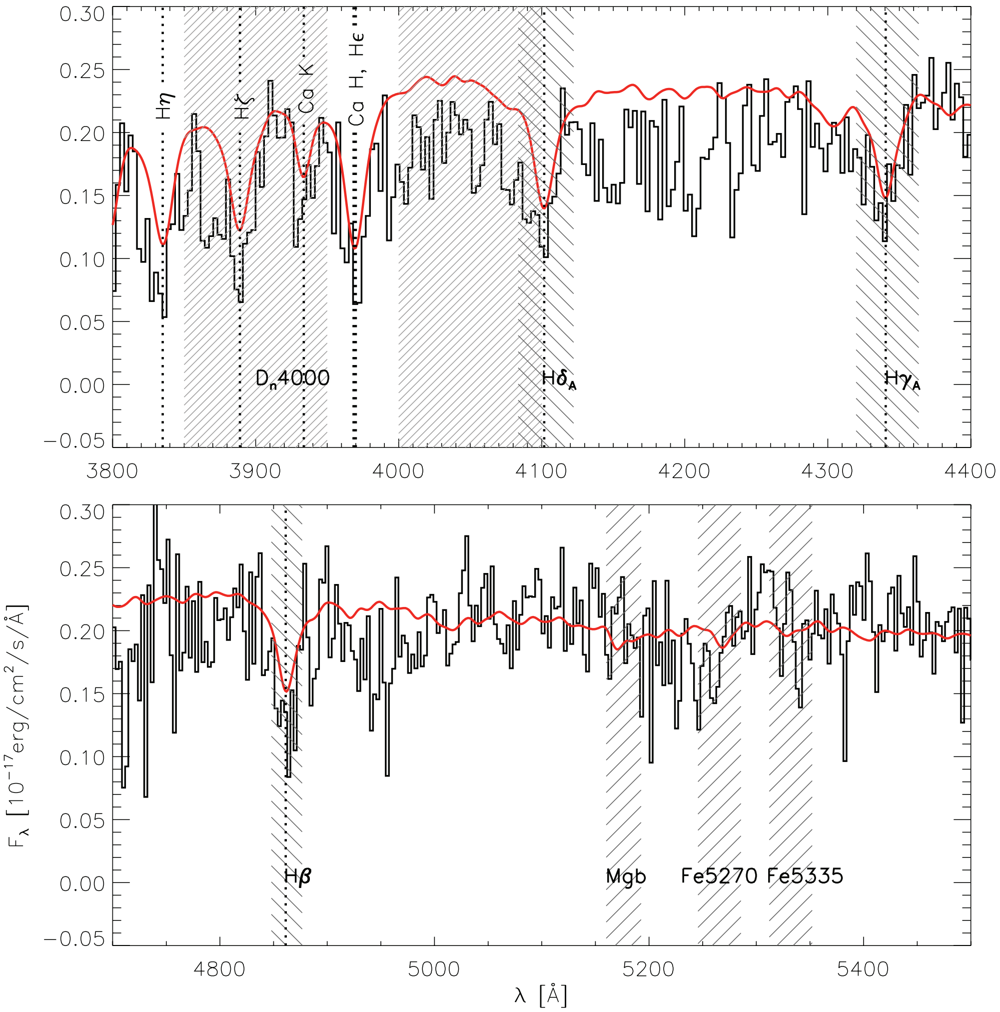

Figure 3. X-shooter spectrum (binned to 3 Å per bin for illustration purposes) zoomed over the region of the absorption indices used in the fit (the two bandpasses defining the 4000 Å break and the central bandpass of the other indices are indicated by the hatched regions). The vertical dotted lines indicate the main absorption features detected. The red spectrum is the best-fit model to the absorption indices, the UV flux ratio, and the observer-frame $J-H$ color.

(A color version of this figure is available in the online journal.)

Table 3
Physical Parameter Estimates and Associated Uncertainties Obtained by Fitting Stellar Absorption Indices, the Rest-frame UV, and Optical Color

Parameter	Estimate	Systematic Uncertainty
$\log(t_r/\mathrm{yr})$	$8.90^{+0.10}_{-0.09}$	0.05 dex
$\log(t_m/\mathrm{yr})$	$9.08^{+0.11}_{-0.10}$	0.03 dex
$\log(Z_*/Z_\odot)$	$0.02^{+0.20}_{-0.41}$	0.06 dex
$\log(M_*/M_\odot)$	$11.37^{+0.13}_{-0.10}$	0.12 dex
τ_V	$1.78^{+0.88}_{-0.63}$	0.33
$\mu\tau_V$	$0.64^{+0.32}_{-0.28}$	0.21
A_{FUV}	$2.52^{+0.89}_{-0.81}$	0.53 mag
A_V	$0.77^{+0.36}_{-0.32}$	0.27 mag

Notes. The parameter estimate is the median of the associated PDF, while the statistical uncertainty is measured from the 16th and 84th percentiles of the PDF. The last column gives the systematic uncertainty estimated by fitting different observational quantities (see Appendix A for details).

we analyze here are chiefly sensitive to age and metallicity and minimally sensitive to dust and α/Fe abundance ratios (this is important because our models have solar-scaled abundances; e.g., Worthey 1994; Thomas et al. 2003) while the colors give constraints on dust attenuation. Specifically, we interpret the stellar absorption indices $D4000_n$, $H\delta_A + H\gamma_A$, and [MgFe]′, the FUV (1300–1780 Å) to NUV (1770–2730 Å) flux ratio, and the observer-frame $J-H$ color. The parameter estimates and associated uncertainties (median and 16th and 84th percentiles of the PDF, respectively) are summarized in Table 3. We derive a luminosity-weighted (mass-weighted) age of 0.8 Gyr (1.2 Gyr) with an accuracy of $\lesssim$30%. The rather weak and low-S/N Mg and Fe features do not allow us to put strong constraints on stellar metallicity which is estimated to be $\log(Z_*/Z_\odot) = 0.02^{+0.2}_{-0.41}$. The relatively large errors on stellar metallicity limit our ability to accurately estimate dust attenuation; however the rather strong 4000 Å break and Balmer absorption lines in combination with the faint and flat UV require a fair amount of dust in this galaxy. The attenuation by dust is estimated to be $A_V = 0.77^{+0.36}_{-0.32}$ in the optical and $A_{\mathrm{FUV}} = 2.5^{+0.9}_{-0.8}$ in the UV. The attenuation in the optical reflects the optical depth in the ISM, $\mu\tau_V$, experienced by stars older than 10^7 yr, while the attenuation in the UV traces well the total effective optical depth τ_V of young stars. Finally, the stellar mass, obtained by normalizing the models to the observed luminosity between the rest frame 5000 and 5800 Å (accounting for dust attenuation), is estimated to be $\log(M_*/M_\odot) = 11.37^{+0.13}_{-0.10}$.

We tested how sensitive the derived parameters are to the observational constraints adopted and found good agreement among the various age estimates and on the need for a significant amount of dust. We note, though, that the inclusion of UV constraints is particularly important for estimating dust attenuation. Our default fit combines the power of absorption features in alleviating parameter degeneracies and the sensitivity of UV and optical colors to dust attenuation. We take the standard deviation of the physical parameters obtained fitting different observational quantities as an estimate of the possible systematic uncertainties. The results are summarized in Table 3 while the comparison between different fitting methods is discussed in Appendix A.

The estimated mass-weighted age of 1.2 Gyr implies that the galaxy must have formed at $z > 3$ ($z_f = 3.2^{+0.5}_{-0.3}$), while the luminosity-weighted age implies that star formation continued at least for other 0.4 Gyr (i.e., until $z \sim 2.7$). We look for the presence of weak nebular emission lines after subtracting the best-fit stellar continuum using the PLATEFIT code (Tremonti et al. 2004).[5] By analyzing the residuals we find a 3σ upper limit to the Hα flux of 3.5×10^{-17} erg s^{-1} cm^{-2}. Adopting the Kennicutt (1998) calibration between SFR and Hα luminosity (SFR[$M_\odot$ yr^{-1}] $= 5.2 \times 10^{-42} L(\mathrm{H}\alpha)$[erg s^{-1}] for the Chabrier IMF), this translates into an upper limit to the current SFR of 5.5 $M_\odot$ yr^{-1}. If we correct the Hα luminosity for the inferred dust attenuation in the optical, the SFR is <10.3 $M_\odot$ yr^{-1} and the specific SFR is $<4.4 \times 10^{-11}$ yr^{-1}.

Finally, we note that the derived stellar metallicity is consistent within the uncertainties with the metallicity of equally massive $z = 0.1$ galaxies (see Gallazzi et al. 2005). The luminosity-weighted age is younger than the local population, as expected, but, if we assume that the galaxy would evolve passively since the redshift of observation until today, its present-day stellar age would be fully consistent with the local age–mass relation.

5. SURFACE BRIGHTNESS PROFILE FITS

We fit the two-dimensional surface brightness profile of the galaxy in the three NIR UDS broadbands J, H and K using GALFIT (Peng et al. 2002). We assumed a Sérsic (1968) model and allowed the Sérsic parameter n, the effective radius r_e, the axis ratio ab, and the position angle P.A. to vary freely. The point-spread functions (PSFs) were estimated from high S/N stacks of stars extracted from the UDS survey (as described in Williams et al. 2010). In Figure 1, we show the K-band image of the galaxy and illustrate the fitting process. There is a foreground ($z_{\mathrm{phot}} = 0.58$) galaxy $\sim$3″ NW of UDS19627, which can potentially influence the fit. We perform three different fits to estimate the uncertainty it introduces: (1) model the two galaxies simultaneously, (2) mask out the foreground galaxy and fit the main galaxy, and (3) model and subtract the secondary galaxy (masking out the main galaxy) and fit the main galaxy in cleaned image. In Table 4, we list the best-fitting parameters of the main galaxy for the three fits. The parameters are slightly sensitive to how the secondary galaxy is taken into account in the fit, but agree within the formal 3σ uncertainties.

We adopt the best-fitting parameters of Fit 1 in the remainder of the paper, and include the standard deviation of the parameters in the three fits in the error estimates, in addition to the formal fitting errors from GALFIT. These parameters are printed in bold face in Table 4. In the same way, we also derive the best-fitting parameters and errors in the H and J bands. The Sérsic parameters agree in the three wavebands. The circularized sizes derived in the H and J bands are slightly larger, but more uncertain and agree within 2σ.

5.1. MIR Emission

The UDS was observed as part of the *Spitzer* UKIDSS Ultra Deep Survey (PI: Dunlop). At 24 μm, the position of UDS19627 is blended with a bright source coinciding with the nearby $z = 0.58$ galaxy (red cross in Figure 1). We model and subtract this source with GALFIT using a bright nearby point source as PSF. The galaxy is not detected in the residual image. In an 7.″5 aperture we derive a flux of 0.1 ± 20 μJy, where we have included the typical error in this size aperture quoted in

---

[5] This code finds the best-fit non-negative linear combination of SSPs and the best-fit dust attenuation that describe the stellar continuum in regions free of emission lines. The best-fit stellar continuum (and any smoothed residuals) is then subtracted from the original spectrum in order to obtain the "pure" emission-line spectrum.

Table 4
Parameters of the Two-dimensional Surface Brightness Distribution Derived with galfit

Fit	Band	Mag	$a_e('')$	n	b/a	χ^2	$r_{e,c}$ (kpc)
1	K	20.24 ± 0.01	0.44 ± 0.01	1.47 ± 0.09	0.74 ± 0.02	0.948	2.77 ± 0.06
2	K	20.18 ± 0.01	0.47 ± 0.01	1.67 ± 0.07	0.77 ± 0.02	0.963	3.04 ± 0.07
3	K	20.26 ± 0.01	0.44 ± 0.01	1.42 ± 0.07	0.73 ± 0.01	1.073	2.70 ± 0.05
Best Fit with Systematic Errors							
1	K	**20.24 ± 0.04**	**0.44 ± 0.02**	**1.47 ± 0.15**	**0.73 ± 0.03**	**0.948**	**2.77 ± 0.11**
1	H	20.54 ± 0.11	0.48 ± 0.05	1.43 ± 0.35	0.81 ± 0.03	0.938	3.24 ± 0.37
1	J	20.99 ± 0.07	0.50 ± 0.03	1.46 ± 0.23	0.80 ± 0.05	0.937	3.20 ± 0.20

Notes. a_e is the effective semimajor axis, n is the Sérsic parameter, b/a is the axis ratio, $r_{e,c} = a_{\rm e,major} * \sqrt{b/a}$ is the circularized effective radius. Fits 1–3 in the three first rows are done in the K band, dealing with the foreground neighbor galaxy in different ways to estimate its effect on the derived parameters of the main galaxy. In Fit 1, the two galaxies are modeled simultaneously. In Fit 2, the main galaxy is fitted with the neighbor galaxy masked out. In Fit 3, the main galaxy is modeled in an image where the neighboring galaxy has first been modeled and subtracted. The errors quoted for the three fits are those returned by galfit. The next three rows, labeled "best fits," are the parameters of the main galaxy from simultaneous fits in the K, H, and J bands. The errors quoted here include the standard deviations from of the best-fitting parameters from Fits 1–3.

the Spuds survey documentation.[6] The non-detection rules out significant amounts of obscured star formation or active galactic nucleus (AGN) activity. Using the method described in Franx et al. (2008), we derive a 2σ upper limit on the star formation rate SFR $\lesssim 40\ M_\odot\ \mathrm{yr}^{-1}$.

6. STELLAR VELOCITY DISPERSION

The presence of several strong stellar absorption features in our spectrum allows for high-quality measurement of the stellar velocity dispersion. This determination is based on the assumption that the observed line broadening is dominated by disordered motions of the stars and that the contribution due to bulk flows or rotation is minimal. We have therefore fitted the spectrum using a set of resolution-matched stellar template spectra to model the effect of the velocity broadening.

6.1. Penalized Pixel Fitting

The public penalized pixel fitting code, pPXF, developed by Cappellari & Emsellem (2004), has been used in the literature to fit velocity dispersions of high-redshift galaxies (e.g., Cappellari et al. 2009; Onodera et al. 2010; van de Sande et al. 2011). We have run pPXF with the MILES empirical stellar library (Sánchez-Blázquez et al. 2006; Falcón-Barroso et al. 2011). As input, pPXF takes the raw X-shooter spectrum (excluding the observed K band) along with all 985 stellar spectra from MILES. We have shifted the observed spectrum to the rest frame, smoothed it with a Gaussian to match the instrumental resolution of the templates, and used logarithmic binning to put all spectra on the same wavelength grid. The code then constructs an optimized linear combination of a small subset of the 985 spectra; in this case, nine templates are chosen and combined. Using only this subset, we have run 1000 fits where the target spectrum is randomized within the errors and the weights for the nine input templates are allowed to vary (including zero weight). The resulting distribution of stellar velocity dispersions is shown in Figure 4. The best-fitting velocity dispersion from this analysis is $\sigma_* = 318 \pm 53$ km s^{-1}.

The inferred velocity dispersion changes in relation to the radii at which it is measured. Using Equation (1) from Cappellari et al. (2006) and assuming that the scaling from the spectrum to the broadband fluxes is only due to missing light from the profile, we infer the correction to σ at r_e to be only a few percent.

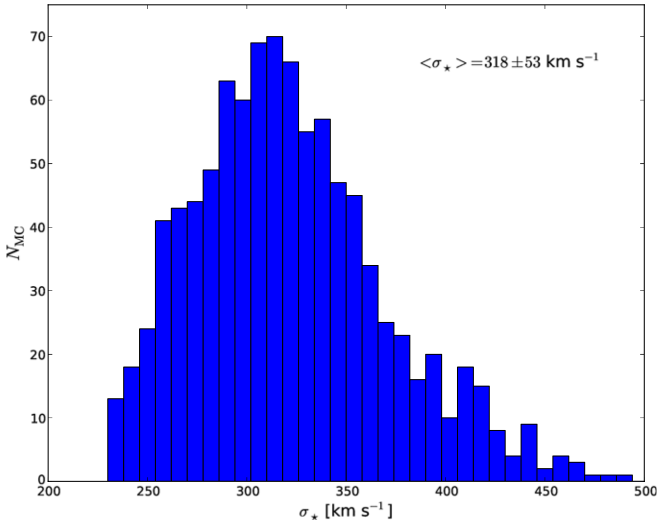

Figure 4. Histogram of best-fit velocity dispersions for the 1000 randomized realizations of the pPXF fitting. Each fit is produced by a new linear combination of the initially chosen nine stellar templates.

(A color version of this figure is available in the online journal.)

We performed an independent test of the derived velocity dispersion through a chi-squared analysis in which we fitted Gaussian convolved, stellar template spectra of five different types (AV, F5V, G8IV, K0III, K0V) observed with X-shooter's UVB arm, which corresponds approximately to the same rest-frame wavelength range as sampled by the NIR arm for the $z = 2$ galaxy. The AV and F5V stars and linear combinations thereof provide good fits with velocity dispersions in the range 260–300 km s^{-1} with typical uncertainty of 50 km s^{-1}, in good agreement with the results from pPXF. The analysis is described in detail in Appendix B.

6.2. Dynamical Mass

We estimate the dynamical mass of the galaxy from the derived velocity dispersion and effective radius (in the K band):

$$M_{\rm dyn} = \beta r_e \sigma_e^2 / G, \tag{1}$$

---

[6] See http://irsa.ipac.caltech.edu/data/SPITZER/SpUDS/documentation/README.txt

Table 5
Properties of the Sample of $z \sim 2$ Quiescent Galaxies with Measured Velocity Dispersions

ID	z	r_e (kpc)	n	$\log(M_*)$ ($M_\odot$)	log(Age) (Gyr)	$\sigma_{\rm obs}$ (km s^{-1})	$\log(M_{\rm dyn})$ ($M_\odot$)	$\sigma_{\rm inf}$ (km s^{-1})
UDS 19627	2.0389	$2.77^{+0.11}_{-0.11}$	$1.47^{+0.15}_{-0.15}$	$11.37^{+0.13}_{-0.10}$	$8.90^{+0.10}_{-0.09}$	318^{+53}_{-53}	$11.51\ ^{+0.11}_{-0.11}$	339
NMBS-C7447	1.800	$1.64^{+0.15}_{-0.15}$	$5.30^{+0.40}_{-0.40}$	$11.18^{+0.20}_{-0.20}$	8.60	294^{+51}_{-51}	$11.23\ ^{+0.11}_{-0.12}$	281
COSMOS-254025	1.820	$2.40^{+0.40}_{-0.40}$	$2.50^{+0.40}_{-0.40}$	$11.54^{+0.06}_{-0.06}$	$9.18^{+0.30}_{-0.18}$	<326	<11.47	354
MUSYC 1252-0	2.186	$0.78^{+0.17}_{-0.17}$	$3.20^{+0.90}_{-0.90}$	$11.36^{+0.04}_{-0.04}$	$9.24^{+0.10}_{-0.13}$	510^{+165}_{-95}	$11.37^{+0.25}_{-0.13}$	469

where β is a constant that depends mainly on the structure of the galaxy. A value of $\beta = 5$ is commonly used in the literature (e.g., Jørgensen et al. 1996). From detailed analysis and modeling of spatially resolved kinematic observations of a sample of 25 local E and S0 galaxies and comparison to detailed modeling of stellar orbits, Cappellari et al. (2006) found that $\beta = 5.0 \pm 0.1$ accurately reproduces galaxy dynamical masses. Adopting this value, we find $M_{\rm dyn} = 3.26 \pm 0.99 \times 10^{11}\ M_\odot$. From simulations it is predicted that β will depend on the structure of the galaxy, increasing with smaller Sérsic n-values (Cappellari et al. 2006). For the best-fitting $n = 1.47$, a value $\beta \sim 7.5$ is predicted. If we adopt this value we find $M_{\rm dyn} = 4.88 \pm 1.49 \times 10^{11} M_\odot$, but as this dependency on structure has not been verified observationally (Cappellari et al. 2006), we will adopt $\beta = 5$ in this paper, which also makes comparison to the literature more straightforward (but see Section 7.8).

6.3. *Spectral Classification of UDS19627*

The spectrum of UDS19627 has the characteristic "shark-tooth" shape of a post-starburst galaxy, consistent with the low derived SFR and constraints on the stellar age and the prominent Balmer series absorption lines. The derived magnitudes (see Table 4) correspond to an $L_K \sim 15\, L_K^*$ galaxy (assuming $K^*_{z=2} = 21.3$; Marchesini et al. 2007). The Sérsic fit to the surface brightness distribution yields a low $n = 1.47$, also more similar to what is found in late-type (and post-starburst) galaxies than what is found in local early types.

7. SAMPLE OF $z \sim 2$ GALAXIES WITH MEASURED VELOCITY DISPERSIONS

Prior to the results presented here, velocity dispersions of three quiescent, massive $z \sim 2$ galaxies have been published. We include the properties of these galaxies in our analysis. Properties of their stellar populations have all been derived assuming a Chabrier IMF. To minimize systematics errors, we recalculate the dynamical masses using effective radii derived from rest-frame optical, and assuming the same value for $\beta = 5$. The observed properties of the $z \sim 2$ galaxies are described in the following and summarized in Table 5.

7.1. *COSMOS-254025*

Onodera et al. (2010) report $\sigma_* < 326$ km s^{-1} derived from a Subaru/MOIRCS spectrum of a $z = 1.82$ galaxy selected from the COSMOS survey. This is an upper limit due to the limited resolution of the spectrograph. Using the results of surface brightness fits by Mancini et al. (2010) ($r_e = 5.79 \pm 0.61$ kpc and $n = 4.14$) from *HST*/ACS F814W-band observations, they derive a dynamical mass of $M < 7 \times 10^{11}\ M_\odot$. For this analysis, we measure the effective radius in NIR images from the UltraVISTA survey (McCracken et al. 2012), sampling the rest-frame optical, which is where the velocity dispersion is measured, and is a better tracer of the stellar mass than the Advanced Camera for Surveys (ACS) I band (rest-frame UV), as $z \sim 2$ galaxies can have strong morphological k-corrections (e.g., Toft et al. 2005; Cameron et al. 2011). Indeed, comparison of the ACS and UltraVISTA images shows that the galaxy is extended and clumpy in the rest-frame UV, but smoother and more centrally concentrated in the rest-frame optical.

Using an identical approach to that described in Section 5 we run GALFIT on the deep J, H, and K-band UltraVISTA survey observations (McCracken et al. 2012), masking out neighboring galaxies, and using a bright nearby star as PSF model, we find a mean effective radius of $r_e = 2.4 \pm 0.4$ kpc and $n = 2.5 \pm 0.4$. The derived r_e is ~60% smaller than the value derived by Mancini et al. (2010) in the F814W band. While the galaxy is only marginally resolved in the UltraVISTA data, sizes measured for galaxies using the procedure followed have been demonstrated to be reliable for galaxies with intrinsic sizes several times smaller than the PSF (Trujillo et al. 2006; Toft et al. 2009) when the galaxy is detected at high S/N and a good PSF model is available, as is the case here. Note that the extent of the galaxy in the ACS image is twice the size of the UltraVISTA PSF (FWHM $\sim 0''.7$), so if the rest-frame optical morphology had been similar it would have been well resolved in the UltraVISTA images.

With our measured r_e the upper limit on the dynamical mass becomes $M_{\rm dyn} < 2.97 \times 10^{11}\ M_\odot$. From the surface brightness fits to the UltraVISTA data we derive an H-band magnitude of 18.42 ± 0.01 and $K = 19.81 \pm 0.01$, corresponding to an $L_K = 22\, L_K^*$ galaxy (Marchesini et al. 2007). From a combined fit of the spectrum and broadband photometry, Onodera et al. (2010) quote a stellar mass of 3–4 × $10^{11}\ M_\odot$, and a luminosity-weighted age of 1–2 Gyr, corresponding to a formation redshift of $z_f = 2.5$–4. The shape of the spectrum is typical of a post-starburst galaxy with prominent Balmer absorption features.

7.2. *NMBS-C7447*

From an X-shooter spectrum of a redshift $z = 1.800$ galaxy in the COSMOS field, van de Sande et al. (2011) derive a velocity dispersion of $\sigma = 294 \pm 51$ km s^{-1}, a dynamical mass $M_{\rm dyn} = 1.7 \pm 0.5 \times 10^{11}\ M_\odot$, and from *HST*/WFC3 observations in the F160W band, an effective radius of $r_e = 1.64 \pm 0.15$ kpc and Sérsic parameter $n = 5.3 \pm 0.4$. The X-shooter spectrum has a typical post-starburst shape, with prominent Balmer lines, and the stellar population synthesis fits to the spectrum are consistent with little ongoing star formation (0.002 $M_\odot$ yr^{-1}), a relatively young age 0.4 Gyr, corresponding to a formation redshift of $z_f \sim 2$, and a stellar mass $1.5 \times 10^{11}\ M_\odot$. In the MUSYC

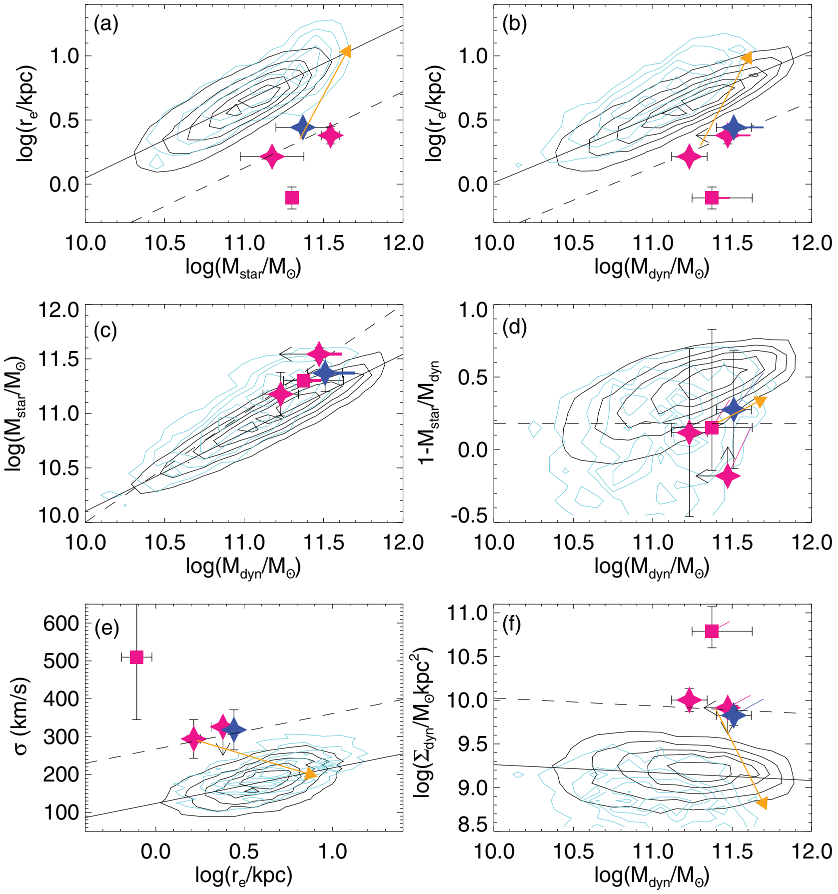

Figure 5. Properties of the four $z \sim 2$ massive quiescent galaxies with measured velocity dispersions, compared to early-type and post-starburst galaxies in the local universe (Blanton et al. 2005; drawn from the SDSS NYU-VAGC). The blue star is the galaxy considered in this paper. The two red stars and the red square are the post-starburst and evolved SEEDs from the literature. The black/cyan contours are low-redshift early-type/post-starburst SDSS galaxies. The full black lines are linear fits to the local galaxies, the dashed lines are linear fits to the high-redshift points, with the slope fixed to the local values. The orange arrows represent the evolution due to merging predicted derived from the cosmological simulations of Oser et al. (2012). The colored lines show the effect on the results of using the expression for $\beta(n)$ of Cappellari et al. (2006) when calculating the dynamical masses rather than assuming $\beta = 5$ (see Section 7.8). (a) Stellar mass vs. effective radius; (b) dynamical mass vs. effective radius; (c) dynamical mass vs. stellar mass; (d) central dark matter fraction ($1 - M_*/M_{\rm dyn}$) vs. dynamical mass; (e) velocity dispersion vs. effective radius; (f) surface (dynamical) mass density vs. dynamical mass.

(A color version of this figure is available in the online journal.)

catalog (Gawiser et al. 2006) it has $H = 19.85$ and $K = 19.75$, corresponding to an $L_K \sim 23\,L_K^*$ galaxy (Marchesini et al. 2007).

7.3. MUSYC 1252-0

van Dokkum et al. (2009) report a $\sigma = 510^{+165}_{-95}$ km s^{-1} derived from a deep Gemini/GNIRS spectrum of a $z = 2.186$ galaxy selected from the MUSYC survey (Gawiser et al. 2006). It has $H = 21.31$, $K = 21.03$, corresponding to an $L = 7\,L_K^*$ galaxy (Marchesini et al. 2007). Based on surface brightness fits to *HST*/NIC2 F160W observations, they find $r_e = 0.78 \pm 0.17$ kpc and $n = 3.2 \pm 0.9$ (van Dokkum et al. 2008). From these numbers, and assuming $\beta = 5$, we calculate $M_{\rm dyn} = 2.4^{+1.9}_{-0.8} \times 10^{11}\,M_\odot$, which is identical to the value quoted in van Dokkum et al. (2009). The shape of the GNIRS spectrum is consistent with an old, evolved, quiescent stellar population, with little ongoing star formation (SFR $\sim$ 1–3 $M_\odot$ yr^{-1}) and age 1.3–2.0 Gyr, corresponding to a formation redshift of $z_f \sim$ 4–7 (Kriek et al. 2009), quite different from the younger, post-starburst spectra of the other three $z \sim 2$ galaxies considered. This galaxy also has a significantly larger velocity dispersion and smaller size than the other three galaxies (see Figure 5).

7.4. Comparison to Low-redshift Galaxies

In Figure 5, we compare the properties of the four $z \sim 2$ galaxies with measured stellar velocity dispersions (colored points) to local $z < 0.2$ early-type (black contours), and post-starburst (cyan contours) galaxies from the Sloan Digital Sky Survey (SDSS) New York University Value-Added Galaxy Catalog (NYU-VAGC; Blanton et al. 2005). The former galaxies are selected using the criteria SFR $< 1\,M_\odot$ yr^{-1} and Sérsic $n > 3$; the latter use the criteria of Goto (2005). Effective radii are measured in the i band.

Three of the $z \sim 2$ galaxies (UDS19627, NMBS-C7447, and COSMOS-254025, represented by stars) follow a mass–size relation with similar slope as for local early-type galaxies, but offset to smaller sizes at a given mass (in the following we will refer to these three galaxies as the post-starburst SEEDs). One galaxy, MUSYC 1252-0 (square), is an outlier with respect to these (we refer to this galaxy as the evolved SEED).

In Figure 5(a), we show the relation between r_e and stellar mass. The $z \sim 2$ post-starburst galaxies follow a relation similar to the local early-type relation (solid line), but offset by a factor of 3.3 ± 0.2 to smaller r_e for a given stellar mass (dashed line). This offset is similar to what has previously been found for larger samples of stellar-mass-selected quiescent galaxies at $z \sim 2$, with photometric masses and redshifts, (e.g., Toft et al. 2009), but smaller than the factor of five offset found for color-selected $z \sim 2$ quiescent galaxies (e.g., Toft et al. 2007; Zirm et al. 2007; Cimatti et al. 2008; van Dokkum et al. 2008), exemplified in these plots by the color-selected MUSYC 1252-0 galaxy. The stellar-mass–size relation of low-z post-starburst galaxies is on average shifted along the early-type relation to larger masses and sizes. In Figure 5(b), we show the same relation for dynamical mass versus effective radius. The $z = 2$ post-starburst galaxies follow a relation similar to the stellar-mass–size relation, but with a smaller offset and scatter. r_e for the $z \sim 2$ post-starburst galaxies are on average 2.5 ± 0.2 times smaller than local early-type galaxies of similar dynamical mass. As illustrated in Figure 5(c), the difference in offset in (a) and (b) is due to a difference in the derived stellar-to-dynamical mass ratio.

For local early-type galaxies there is a tight correlation between $M_{\rm dyn}$ and M_*, with the ratio of dynamical-to-stellar mass (within r_e) increasing from the least massive to the most massive galaxies (see also Padmanabhan et al. 2004; Gallazzi et al. 2006; Taylor et al. 2010). Under the assumption of structural homology, this can be interpreted as an increasing dark matter fraction with mass. The local galaxies with $\log(M_{\rm dyn}/M_\odot) \sim 10.5$ are thus baryon dominated, while the most massive, $\log(M_{\rm dyn}/M_\odot) > 11.5$, have much larger dark matter fractions. A similar trend has been shown to be valid in early-type galaxies out to $z \sim 1$ (e.g., Ferreras et al. 2005; Rettura et al. 2006). While the $z \sim 2$ galaxies are consistent with the local relation within the error bars, it is striking that the best-fitting values all fall close to the dashed line ($M_* = M_{\rm dyn}$), indicating a lower dark matter fraction than in similar mass early-type galaxies at lower redshift. We explore this further in Figure 5(d) where we plot $1 - M_*/M_{\rm dyn}$: a proxy of dark matter fraction as a function of dynamical mass (assuming homology). The central dark matter fractions of the $z \sim 2$ galaxies scatter around a mean value $1 - M_*/M_{\rm dyn} = 0.18 \pm 0.20$, while the low-redshift galaxies in the same dynamical mass range have a mean of 0.46 ± 0.23. Note from (b) that the dynamical-mass–size relation of the local post-starburst galaxies is shifted from the early-type relation to larger sizes at a given mass. From plots (c) and (d), it can be seen that the low dark matter fraction found in the $z \sim 2$ galaxies is consistent with what is found in local post-starburst galaxies, which show a large range in $M_*/M_{\rm dyn}$, but on average have $M_{\rm dyn} \sim M_*$. The observed low central dark matter fraction of the $z \sim 2$ galaxies compared to that in local early-type galaxies could have implications for the evolutionary path to lower redshift. We explore this further in the discussion (Section 8).

In Figure 5(e), we plot the effective radius versus the velocity dispersion. The average velocity dispersion of the $z \sim 2$ post-starburst galaxies is 1.8 ± 0.5 times larger than in low-redshift galaxies of similar size, while the velocity dispersion of MUSYC 1252-0 is 4.1 ± 2.1 times larger than local galaxies of similar size. The local post-starburst galaxies have a similar distribution as local early types but shifted to larger sizes and velocity dispersions.

In Figure 5(f) we plot the inferred (dynamical) mass density within the effective radius $\Sigma = 0.5\, M_{\rm dyn}/(\pi r_e^2)$ versus the dynamical mass $M_{\rm dyn}$. The $z \sim 2$ post-starburst galaxies have average surface mass densities 5.8 ± 1.2 times higher than the mean in local early types of similar mass. The relations for the local post-starburst galaxies are shifted to smaller surface mass densities. As in the dynamical-mass–size plot, the offset of the $z = 2$ post-starburst galaxies from the local post-starburst relation is similar to the offset of the evolved $z = 2$ galaxy from the local early-type relation.

7.5. *Evolution through Merging?*

Dry merging has been suggested as a mechanism to "puff up" the SEEDs and evolve them into agreement with the mass–size relation observed at low redshift (Naab et al. 2007, 2009; Bezanson et al. 2009; Newman et al. 2011). Previous studies of the stellar-mass–size relation have not been able to unambiguously distinguish between different merging scenarios, but minor merging is the most promising process. With the added dynamical information, we can now start to test different merger scenarios in greater detail than is possible with just stellar masses and sizes. The low inferred dark matter fraction of the $z \sim 2$ galaxies, compared to early types at low redshift, supports the merging scenario, as merging can redistribute the dark matter within the effective radius (Boylan-Kolchin et al. 2005; Oser et al. 2012). Furthermore, if the dark matter profile is more radially extended than the stars, increasing r_e by adding stars in the outskirts can lead to an increased measured dark matter fraction by up to a factor of 2–3 because areas with higher dark matter content are included within the effective radius (M. Hiltz et al., in preparation, T. Naab 2012, private communication).

Based on simple virial arguments, Bezanson et al. (2009) and Naab et al. (2009) show that dry merging can lead to an increase in size of the remnant, and that minor merging is likely to be the dominant process, as this is the most efficient process for size growth, in terms of added mass needed for the observed size evolution (about a factor of two). Recent semi-analytical models suggest that minor mergers can account for most of the observed size evolution between $z = 2$ and 0, but not all, especially between $2 < z < 1$ where the required evolution is largest (Newman et al. 2010; Shankar et al. 2011; Cimatti et al. 2012).

Cosmological simulations studying the effect of merging on the size evolution of massive galaxies show that the dominant mode of mass growth is minor merging, with a typical mass-weighted ratio of 1:5 (Oser et al. 2012). The average integrated size growth between $z = 2$ and 0 for $M \sim 10^{11}\ M_\odot$ galaxies in these simulations is a factor of 5–6, and an average mass growth of a factor of 2.1. The velocity dispersion in the remnants is approximately 30% lower than in their progenitors at $z = 2$. This evolution is almost identical to what is predicted from the simple virial approximations for a similar mass growth. Interestingly, in these simulations galaxies at $z = 2$ typically have low dark matter fractions at $z = 2$ (0.1–0.3, similar to what is derived here for the observed $z \sim 2$ galaxies), and these increase with time as a consequence of the merging by approximately a factor of two. In Figure 5, we plot with arrows the evolution from the cosmological simulations of Oser et al. (2012). For the $z \sim 2$ post-starburst galaxies, these predictions provide a good match to the observed evolution of the stellar-mass– and velocity–size relations. However, they slightly overpredict the evolution in the dynamical-mass–size and dynamical-mass-density–mass relations where the galaxies end up on the outskirts, rather than on the mean, of the local relations, as a consequence of the evolution of dark matter fraction in the simulations not being sufficient to account fully for the observed evolution (assuming that the dark matter fraction of the $z \sim 2$ galaxies evolves into those found in typical local elliptical galaxies). For the evolved $z \sim 2$ galaxy, additional structural evolution is needed. Some of the additional evolution needed in the dark matter fraction may be attributed to merging with galaxies with higher dark matter fractions than those included in the simulations. In the local universe dwarf galaxies can be heavily dark matter dominated, with stellar masses $\sim 10^7\,M_\odot$ and dynamical masses $\sim 10^8$–$10^9\,M_\odot$, corresponding to dark matter fractions as high as 95% (e.g., Carignan & Beaulieu 1989; Persic et al. 1996; Strigari et al. 2010). If the $z \sim 2$ galaxies grow via minor merging with primarily dark-matter-dominated dwarfs, it could be an efficient way of increasing the dark matter fraction in the remnant.

7.6. The Fundamental Plane at $z \sim 2$

Previous studies of the evolution of the FP have been limited to galaxies at $z \lesssim 1.3$, where velocity dispersions can be derived from absorption lines in the observed optical (van der Wel et al. 2004; di Serego Alighieri et al. 2005; Martinez-Manso et al. 2011)

From the measured velocity dispersions, effective radii, and the mean rest-frame surface brightness within the effective radius,

$$\langle \mu_e \rangle = V_z - 5\log(r_e) + 2.5\log(2\pi) - 2.5\log((1+z)^4) - A_V, \quad (2)$$

we can for the first time probe the FP of $z \sim 2$ quiescent galaxies:

$$\log(r_e) = \alpha \log(\sigma) - \beta \log(I_e), \quad (3)$$

where V_z is the (AB) magnitude in the redshifted V band, which following van Dokkum & Franx (1996) can be estimated simply as $V_z = H + 2.5\log(1+z)$ (since the observed H band resembles closely the V band redshifted to $z \sim 2$), r_e is the (H-band) effective radius, σ is the velocity dispersion in km s^{-1}, and $I_e = 10^{(-0.4*\mu_e)}$.

Here we adopt $\alpha = 1.2$ and $\beta = 0.83$, as derived by Jørgensen et al. (1996) for a sample of 225 galaxies in 10 nearby clusters. Note that this quite strong assumption for the three-dimensional orientation of the fundamental plane essentially builds in homologous evolution in the following analysis, but it's the best we can do given the paucity of $z \sim 2$ data points.

In Figure 6, we compare the rest-frame V-band FP of the $z \sim 2$ galaxies to the FP observed locally in the $z \sim 0.02$ Coma cluster (Lucey et al. 1991) and in the $z \sim 0.33$ cluster CL1358+62 (Kelson et al. 2000). The galaxies have been corrected for cosmological $(1+z)^4$ surface brightness dimming. The slope of the $z = 0.33$ FP is similar to that in the Coma cluster, but slightly offset.

While it is not possible to derive robust estimates of slope or scatter of the $z \sim 2$ galaxies, we note that they show a significantly larger scatter than the local relation, and a large offset from it. As in Figure 5, the evolved and the post-starburst $z \sim 2$ galaxies fall in different parts of the plot. Assuming the local slope, the post-starburst galaxies are on average offset by 1.6 ± 0.2 dex from the local relation. The evolved SEED is closer to the local relation.

As the velocity dispersion traces the total mass, and the surface brightness traces the light, the offset between the fundamental planes at different redshifts is often interpreted as an offset in mass-to-light ratio caused by passive aging of the stellar populations, which shifts the plane up as the surface brightness fades, while the velocity dispersion stays the same (e.g., van Dokkum & van der Marel 2007).

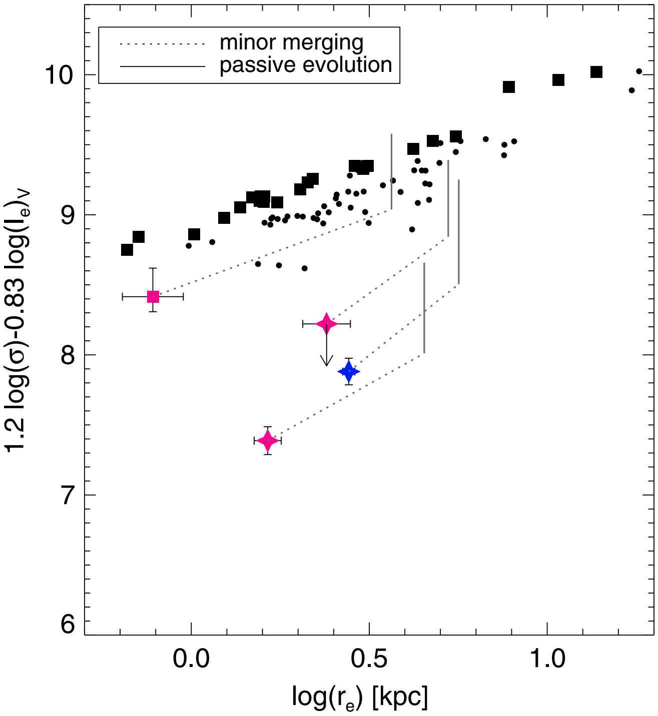

Figure 6. Comparison of the rest-frame V-band fundamental plane of the $z \sim 2$ galaxies compared to that in the $z = 0.02$ Coma cluster (black squares; Lucey et al. 1991) and in the $z = 0.33$ cluster CL1358+62 (black circles; Kelson et al. 2000). The stars are the post-starburst SEEDs, with the blue star the one considered in this paper; the square is the evolved SEED. The $z = 2$ galaxies are offset significantly from the local relation. The lines indicate the effect of luminosity and structural evolution considered between $z = 2$ and 0. The dotted and dashed lines are the evolution predicted by the minor and major merging scenarios in Section 7.4, and the full line is the effect of passive evolution of the M/L predicted by the best-fitting stellar population synthesis models between their observed redshift and today, assuming the best-fitting formation redshift, z_f, a Chabrier IMF, and solar metallicity. These combined evolutionary effects are able to bring the evolved SEED close the local fundamental plane, but cannot fully account for the offset of the post-starburst SEEDs.

(A color version of this figure is available in the online journal.)

The offset observed for the $z = 2$ post-starburst galaxies is too large to be explained by passive evolution. The solid lines represent the maximum evolution of the surface brightness that can be attributed to passive aging of the stellar population between $z = 2$ and $z = 0$, assuming solar metallicity, a Chabrier IMF, and that the stars were formed in a single stellar burst at their derived z_f. We note that this relies on the ages being correct. If these are systematically overestimated there could be room for more passive evolution. It is clear that in order to end up on the local relation the galaxies also have to go through structural evolution. The minor merging scenario described above would also have an effect on the FP as it changes the velocity dispersion and size, and thus also the surface brightness, of the galaxies. Studies of the FP at $z \sim 1$ suggest that minor merging is needed in addition to passive evolution to explain the offset from the local relation (van der Wel et al. 2004; di Serego Alighieri et al. 2005; Martinez-Manso et al. 2011). The expected shift of the $z \sim 2$ galaxies due to this process is indicated with dotted lines. These evolutionary effects in concert bring the $z = 2$ post-starburst galaxies closer to the local relation but still systematically under it. The offsets range from 0.2 to 1 dex (with a mean of 0.5 ± 0.4). Interestingly, the evolved SEED ends up on the local relation through these processes; however from Figure 5 we know that it needs to go through additional structural evolution to end up on the local mass–size relation.

A possible origin of the additional offset from the local FP that cannot be accounted for by passive evolution and minor merging is that the evolution between $z = 2$ and 0 may be non-homologous.[7] This is not unlikely as we know that at least some of the $z = 2$ galaxies have to change their surface brightness profiles from exponential disk to deVaucouleurs profiles. Local post-starburst galaxies have in some cases been shown to be offset by a similar amount from the FP, which is attributed to much younger stellar ages of those particular galaxies (Yang et al. 2004). Similarly, at $z \sim 1$, post-starburst galaxies are offset more from the local FP than elliptical galaxies (van der Wel et al. 2004). However this is not a likely explanation for the additional offset of the $z = 2$ galaxies, as the effect of younger stellar populations has been taken into account when calculating the maximum passive evolution of the galaxies between $z = 2$ and 0. Metallicity and/or age gradients in the $z \sim 2$ galaxies could be a potential source of uncertainty; however higher resolution multicolor imaging is needed to address this.

7.7. Clues to the Formation Mechanism of SEEDs

The observations presented here hold important clues to the formation scenario of SEEDs which is still not well understood. The uniformly old and extremely compact stellar populations suggest that the majority of the stars formed in a major nuclear starburst at high redshift. Simulations indicate that highly dissipational processes on short timescales are plausible mechanisms for creating the compact stellar populations (e.g., Naab et al. 2007, 2009). A possible scenario is major gas-rich mergers at high redshift (Wuyts et al. 2010), in which the gas is driven to the center, igniting a massive nuclear starburst ($>1000\ M_\odot\ \mathrm{yr}^{-1}$), followed by an AGN/QSO phase which quenches the star formation, and leaves behind a compact remnant (Hopkins et al. 2006). Submillimeter galaxies (SMGs)/ultraluminous infrared galaxies may be examples of this process in action. Observations show that most of them are major mergers, with large amounts of dust-enshrouded star formation and high central concentrations of molecular gas, comparable to the density of stars in SEEDs (Greve et al. 2005; Tacconi et al. 2006, 2008; Michałowski et al. 2012). The compact structure, post-starburst nature, and (at least in the case of the galaxy studied here) relatively high extinction make them very likely descendants of $z > 3$ dusty SMGs. With the accurate ages obtainable from NIR spectroscopy of quiescent $z \sim 2$ galaxies, we can begin to constrain the number densities of their progenitors as a function of redshift: e.g., if one assumes a direct evolutionary link between quiescent $z \sim 2$ galaxies and $z > 4$ SMGs their relative number densities can be used to constrain the duty cycle of star formation to be ~50 Myr (Capak et al. 2008).

7.8. Caveats

As the $z \sim 2$ galaxies are spatially unresolved in the spectroscopic observations, it is not possible to determine if some of the broadening of the absorption lines, which we interpret as velocity dispersion, could be due to rotation. This may be a likely scenario given that some of their surface brightness profiles are best fitted by exponential-disk-like profiles, and there is evidence from recent high-resolution observations that a significant fraction of SEEDs may have flattened disk-like morphologies (van der Wel et al. 2011). This could lead to a systematic bias in their velocity dispersions and dynamical masses. This, in turn, would mean that the derived offset from the local dynamical-mass–size relation could be biased. Other sources of possible uncertainties in the dynamical masses are that the assumptions of homology and isotropy, needed to calculate the dynamical mass from the velocity dispersion, may not be fully valid. Some studies have suggested that the sizes of compact $z \sim 2$ galaxies could be underestimated due to faint profile wings not detected due to cosmological surface brightness dimming (e.g., Mancini et al. 2010), which would lead to the dynamical masses being underestimated. However, considering the bright magnitudes of the galaxies considered in this paper, and that ultra deep studies tracing the surface brightness profile of compact $z \sim 2$ galaxies out to $>10r_e$ have failed to detect such wings (e.g., Szomoru et al. 2010, 2011), this is not likely to be a very significant effect compared to the other potential systematic errors.

The derived low dark matter fraction is sensitive to the $\beta = 5$ assumption made when calculating the dynamical masses. From theory, it is predicted that β should depend on the structure of the galaxies in a way that can be approximated through the following dependency on the Sérsic n parameter: $\beta = 8.87 - 0.831n + 0.024n^2$ (Cappellari et al. 2006). The colored lines in Figure 5 shows the effect of assuming this $\beta(n)$ correlation. The dynamical masses increase 3%–50% for the $z \sim 2$ galaxies, resulting in a higher mean average dark matter fraction (0.29 ± 0.18). However, Cappellari et al. (2006) showed that there is no observational support for this correlation and real galaxies (with $n = 2$–10) are best fitted by $\beta \sim 5$; we therefore adopt this value.

Another potential uncertainty is the IMF assumed in the stellar population synthesis modeling. Theoretical and observational studies have argued that the IMF may depend on redshift and/or environment (e.g., Blain et al. 1999; Tumlinson 2007; van Dokkum 2008; Wilkins et al. 2008; Treu et al. 2010). If that is the case, assuming the same IMF for the $z = 2$ and $z = 0$ galaxies may introduce a bias in the estimated stellar masses. Observations of $z < 1$ massive early-type galaxies acting as gravitational lenses suggest that a Salpeter IMF provides a better fit than a Chabrier IMF (e.g., Grillo et al. 2009; Auger et al. 2010; Sonnenfeld et al. 2011). Assuming a Salpeter IMF rather than an Chabrier IMF for the $z \sim 2$ galaxies would lead to approximately 1.75 times higher stellar masses (e.g., Gallazzi et al. 2008), resulting in stellar masses significantly higher than the dynamical masses, strongly disfavoring a Salpeter IMF for the $z \sim 2$ galaxies. The derived stellar masses of the $z \sim 2$ galaxies have a relatively weak dependance on whether or not the IMF is bottom light at the observed stellar ages (~1–2 Gyr, Marchesini et al. 2009), but at the older ages of local galaxies (~10 Gyr) the derived stellar mass is more sensitive to the underlying IMF, leading to a potential bias between the $z = 2$ and $z = 0$ mass–size relations. As a consistency check, we calculate the so-called inferred velocity dispersion from the stellar mass and effective radius: $\sigma_{\mathrm{inf}}^2 = GM_*/\beta r_e$. The derived σ_{inf} for $z \sim 2$ agrees well (within ~10%) with the measured velocity dispersions (as expected since $M_{\mathrm{dyn}} \sim M_*$, see Table 5).

As evident from Figure 1, UDS19627 is located close to a foreground galaxy (angular separation $\theta = 2\farcs83$). This galaxy is responsible for a gravitational lensing effect that causes a bias in the derived brightness, derived stellar mass, size, and dynamical mass of the $z \sim 2$ background galaxy. To estimate this effect we construct a simple lensing model of the system. We assume for the foreground galaxy a photometric redshift

---

[7] The adopted merging scenario of Oser et al. (2012) includes non-homologous evolution, but the adoption of the local three-dimensional orientation of the FP assumes homology.

$z_l = 0.58$ and stellar mass $\log(M_{*,l}/M_\odot) = 10.32^{+0.07}_{-0.05}$, where both values are derived from broadband B, r, i, z, J, and K-band photometry, using the same model library as for our main target. We then compare this stellar mass value to those of the SLACS lens galaxies (Bolton et al. 2006; Grillo 2010) to estimate the effective velocity dispersion $\sigma_{\rm SIS}$ of a singular isothermal sphere (SIS) model that we adopt here to describe the total mass distribution of the lens. We find that a value of 145 km s^{-1} would be typical for lens galaxies with stellar mass values similar to that of our foreground galaxy. For an SIS model, we recall that the Einstein radius $\theta_{\rm Ein}$ is given by

$$\theta_{\rm Ein} = 4\pi(\sigma_{\rm SIS}/c)^2\, D_{\rm ls}/D_{\rm os}, \tag{4}$$

where c is the speed of light and $D_{\rm ls}$ and $D_{\rm os}$ are the angular diameter distances between the lens and the source and the observer and the source, respectively. The magnification factor μ at an angular distance θ, that is larger than $\theta_{\rm Ein}$, from the center of the lens is given by

$$\mu(\theta) = 1 + \theta_{\rm Ein}/(\theta - \theta_{\rm Ein}). \tag{5}$$

Following the previous two equations, we calculate a magnification factor of 10%–20% for the $z \sim 2$ galaxy. The brightness and stellar mass are thus overestimated by this amount and the size by the square root of this. By applying this correction, we would get a 0.07 dex lower stellar mass and a 0.03 dex lower dynamical mass. Given the relatively small weight of the lensing effect compared to the other uncertainties in our analysis and the approximations adopted in the lensing modeling, we decide not to correct our results for the lensing effect. We note that lensing is likely to be a general issue that needs to be taken into account when analyzing samples of the very brightest $z \sim 2$ quiescent field galaxies.

8. SUMMARY AND DISCUSSION

Since their initial discovery (Toft et al. 2005, 2007; Daddi et al. 2005; Trujillo et al. 2006; Zirm et al. 2007) the extreme properties of SEEDs have been heavily debated, as galaxies with such properties were not expected from galaxy evolution models and are very rare in the local universe (Trujillo et al. 2009; Taylor et al. 2010; Shih & Stockton 2011; Ferré-Mateu et al. 2012). Initial worries that their large inferred mass densities could be caused by observational biases and/or systematic uncertainties in their derived sizes have since been ruled out through larger, better-defined samples with increasingly deeper, higher resolution imaging (e.g., Cimatti et al. 2008; van Dokkum et al. 2008; Toft et al. 2009; Damjanov et al. 2011; Szomoru et al. 2011). With new, more sensitive NIR spectrographs like X-shooter, we are now entering an exciting era where it is becoming possible to detect absorption lines at sufficient S/N and resolution to constrain their relative strengths, which are sensitive to the age and metallicity of the stellar populations, but not to dust content, and their broadening, from which we can derive the velocity dispersion and dynamical mass.

In this paper, we presented the first spectrum of a massive evolved $z \sim 2$ galaxy of sufficient S/N and resolution to perform detailed absorption line spectroscopy. From the absorption lines, we derive a velocity dispersion of $\sigma_* = 318 \pm 53$ km s^{-1} and a dynamical mass of $\log(M_{\rm dyn}/M_\odot) = 11.51 \pm 0.11$. Simultaneous fits to absorption line indices and the full rest-frame UV–optical spectrum allowed us, for the first time at $z \sim 2$, to break the degeneracies between age, dust, and metallicity, resulting in more realistic error bars on all derived quantities, including the stellar mass.

- We derived a metallicity of $\log(Z_*/Z_\odot) = 0.02^{+0.2}_{-0.41}$, which is comparable to that of similar mass local galaxies.
- We accurately determined the mass/luminosity-weighted stellar age (to within 0.1 dex), which implies that the majority of the stars formed in a burst at $z_f > 3.3^{+0.5}_{-0.3}$ which continued for at least another 0.4 Gyr (to $z \sim 2.7$). The derived mean stellar age is naturally much younger than in local galaxies, but if the galaxy evolves passively to the present day, its stellar age will be similar to local galaxies of similar mass.
- We independently confirmed the galaxies' quiescent nature by deriving robust upper limits on the specific SFR from the slope of the UV continuum and upper limits on emission lines: sSFR $< 4.4 \times 10^{-11}$ yr^{-1}. The shape of the continuum and the presence of strong Balmer absorption lines resemble a mix of A and F stars, typical of post-starburst galaxies and consistent with the galaxy being quiescent, but with a significant starburst relatively recently.

We compiled three additional spectroscopically confirmed massive quiescent $z \sim 2$ galaxies with measured velocity dispersion and dynamical masses from the literature, allowing for a homogeneous study of scaling relations between structural and dynamical properties of evolved galaxies at this high redshift.

Two of the galaxies are also post-starburst galaxies with similar ages ($\lesssim 1$ Gyr), brightnesses ($L_K = 15$–$23\ L_K^*$), velocity dispersions, and sizes to the galaxy analyzed in this paper, while one is less luminous ($L_K = 7\ L_K^*$) and much more compact. This galaxy has a spectrum characteristic of more evolved stellar populations, with less prominent Balmer lines, but stronger Ca H and K absorption lines, and an estimated age of >1.5 Gyr. The $z \sim 2$ post-starburst galaxies are not as compact as the typical quiescent $z \sim 2$ galaxies studied previously in photometric samples. This may be a selection effect, as they were selected for spectroscopy due to their brightness and are therefore likely to be biased toward younger, less evolved $z \sim 2$ quiescent galaxies, where the brightnesses have been boosted by a starburst in the not-so-distant past. The evolved SEED MUSYC 1252-0 is an outlier in this paper, but may be more representative of the quiescent $z \sim 2$ galaxy population, with a fainter K-band magnitude, older stellar population, and higher stellar mass density. The sample allowed for:

- The study of the dynamical-mass–size relation of quiescent galaxies at $z \sim 2$, which is independent of systematic uncertainties and degeneracies introduced by photometric redshifts and stellar population synthesis modeling of broadband photometry.
- The offset of the dynamical-mass–size relation of the $z = 2$ post-starburst galaxies from the local early-type relation is smaller (a factor of 2.5) than the offset of the stellar-mass–size relation (a factor of 3.3), and its scatter appears to be smaller (though this is hard to quantify, given the small sample).
- The smaller offsets are caused by a difference in stellar-to-dynamical mass ratios of the SEEDs and the local early-type comparison sample. Interpreting this as a difference in the central dark matter fraction, the latter on average have a dark matter fraction of 0.46 ± 0.23 while the SEEDs on average have a dark matter fraction of 0.18 ± 0.20, consistent with being completely baryon dominated.

We also compared the $z \sim 2$ galaxies to local post-starburst galaxies.

- The local post-starburst stellar-mass–size relation is similar to the local early-type relation, but shifted along the relation to higher masses and larger sizes. The local post-starburst population shows a shift between the stellar- and dynamical-mass–size relations, similar to the $z \sim 2$ post-starburst galaxies, indicating a similarly low central dark matter fraction.

We compared the observed structural and dynamical properties of our $z \sim 2$ sample to predictions from the cosmological simulations of Oser et al. (2012) for the size, velocity dispersion, and dark matter fraction evolution of massive galaxies between $z = 2$ and $z = 0$. The simulations do a qualitatively good job in reproducing the difference in the stellar-mass–size relations, and the size–velocity dispersion relations, and are also able to reproduce some (around 50%) of the observed difference in dark matter fraction between $z = 2$ and 0, but not all of it, resulting in the galaxies ending up on the outskirts, rather than on the mean local dynamical-mass–size relation. The observed low dark matter fractions are also in qualitative agreement with recent semi-analytical models which predict that the dark matter fraction in massive spheroids should decrease with redshift (Shankar et al. 2011).

To further compare the structural properties of the $z \sim 2$ sample to local galaxies, we constructed:

- The first estimate of the FP at this high redshift, which is offset from the local FP by a larger amount than can be explained by passive evolution of the stellar populations; in other words, they have to go through structural evolution to evolve onto the FP observed at lower redshift.

The structural evolution implied by the cosmological simulations brings the $z = 2$ galaxies closer to the local FP, but still significantly offset. This suggests that additional, possibly non-homologous structural evolution is needed. A possible mechanism responsible for this evolution is major mergers: observations show that most massive galaxies will undergo at least one major merger between $z = 3$ and 0 (e.g., Man et al. 2012), and while this may not be an efficient mechanism for size growth (e.g., Bezanson et al. 2009), it could increase the central dark matter fraction (through redistribution of the dark matter; Boylan-Kolchin et al. 2005) and provide some of the structural evolution needed (e.g., changing the structure from disk like to bulge like).

It has been suggested that SEEDs are more compact than galaxies of similar mass assembled later in the history of the universe, because the universe was much denser and more gas rich at earlier times (e.g., Khochfar & Silk 2006). If this is the case we may expect the mass density of SEEDs to be larger for older, more evolved examples than for younger ones. Zirm et al. (2012) suggested that the peak stellar density may scale with their formation redshift while the ratio of high-density to low-density components would be related to the number of (dry) mergers they have undergone. In Figure 7, we plot the central (dynamical) mass density of the $z \sim 2$ galaxies versus their estimated formation redshift. Based on these four galaxies alone it is not possible to determine if there is a relation, but we note that the post-starburst SEEDs have similar mass density and formation redshift, which are both significantly smaller than in the evolved SEED, consistent with this scenario. The main uncertainty in the plot is the lack of accurate ages/formation redshifts with realistic error bars for the three galaxies from the literature. The papers describing the observations only give rough ranges of possible ages for two of them, while for one (NMBS-C7447) no errors on the age are quoted. In a recent work on a photometric sample of quiescent galaxies at $z \sim 2$, Szomoru et al. (2011) did not find a relation between compactness and rest-frame $U-V$ color, which was used as a proxy for stellar age. However, we cannot rule out that this may be due to inaccuracy of the adopted age proxy. As shown in this paper, careful analysis of the absorption lines' strength and the continuum emission in X-shooter spectra allows for much more accurate age estimates, making it possible to observationally test for such a relation. SEED galaxies are excellent targets for this test. They are quiescent with SFHs well fitted by models with relatively well-defined formation redshifts and they have regular symmetric morphologies, making it relatively simple to accurately determine their mass density.

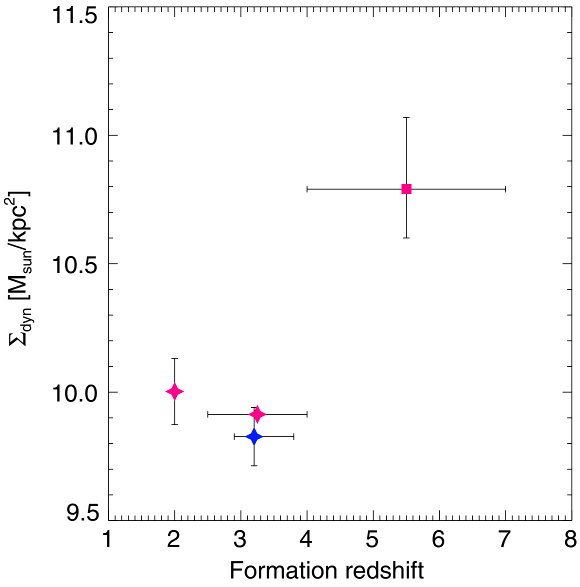

Figure 7. Dynamical mass density vs. the mean stellar formation redshift for the $z \sim 2$ galaxies. The formation redshift is calculated from the stellar ages, derived from the stellar population synthesis fits to the spectra. The error bars on the mean formation redshifts of the three galaxies from the literature are tentative, as they are not accurately derived in the papers (in one case missing). This small sample is consistent with a picture where galaxies formed at higher redshift are denser.

(A color version of this figure is available in the online journal.)

In this paper we have presented homogeneous constraints on the $z \sim 2$ dynamical-mass–size relation, the first constraints on the FP, and a possible relation between stellar age and compactness, relations that have until now only been possible to study out to $z \sim 1.3$. In the immediate future, it will be possible to put such and related studies on a secure statistical footing as the samples of $z \sim 2$–3 quiescent galaxies with absorption line spectroscopy increase. This will be a large leap forward in our understanding of galaxy formation, as this is the era where these and other scaling relations we observe at lower redshift are believed to form.

We thank Lise Christensen, Tayyaba Zafar, and Marijn Franx for sharing their experience with X-shooter observations and data reduction; Ryan Quadri and Rik Williams for assistance with the target selection, and for providing their UDS catalogs and images; Thorsten Naab for useful discussions related to predictions from cosmological simulations; Jens Hjorth for care-

Table 6
Stellar Population Parameter Estimates and Uncertainties Obtained by Fitting Different Observational Constraints

Method	$\log(t_r/\mathrm{yr})$	$\log(t_m/\mathrm{yr})$	$\log(Z_*/Z_\odot)$	$\log(M_*/M_\odot)$
(1) indices, UV and $J-H$ color	$\mathbf{8.90^{+0.10}_{-0.09}}$	$\mathbf{9.08^{+0.11}_{-0.10}}$	$\mathbf{0.02^{+0.20}_{-0.41}}$	$\mathbf{11.37^{+0.13}_{-0.10}}$
(2) indices, $J-H$	$8.94^{+0.10}_{-0.09}$	$9.11^{+0.10}_{-0.11}$	$-0.02^{+0.23}_{-0.45}$	$11.30^{+0.12}_{-0.11}$
(3) indices, UV flux ratio	$8.93^{+0.11}_{-0.10}$	$9.10^{+0.11}_{-0.11}$	$0.03^{+0.19}_{-0.41}$	$11.47^{+0.20}_{-0.16}$
(4) full SED	$9.01^{+0.14}_{-0.14}$	$9.15^{+0.12}_{-0.14}$	$0.04^{+0.20}_{-0.40}$	$11.56^{+0.17}_{-0.19}$
(5) indices, color excess	$8.99^{+0.10}_{-0.11}$	$9.13^{+0.10}_{-0.13}$	$-0.09^{+0.28}_{-0.38}$	$11.29^{+0.08}_{-0.09}$
	τ_V	$\mu\tau_V$	A_{FUV}	A_V
(1) indices, UV and $J-H$ color	$\mathbf{1.78^{+0.88}_{-0.63}}$	$\mathbf{0.64^{+0.32}_{-0.28}}$	$\mathbf{2.52^{+0.89}_{-0.81}}$	$\mathbf{0.77^{+0.36}_{-0.32}}$
(2) indices, $J-H$	$1.37^{+0.81}_{-0.72}$	$0.40^{+0.34}_{-0.23}$	$1.83^{+0.93}_{-0.79}$	$0.49^{+0.39}_{-0.28}$
(3) indices, UV flux ratio	$2.04^{+1.01}_{-0.66}$	$0.83^{+0.45}_{-0.36}$	$3.04^{+1.19}_{-0.98}$	$0.98^{+0.50}_{-0.41}$
(4) full SED	$2.10^{+1.024}_{-0.74}$	$0.85^{+0.46}_{-0.43}$	$3.09^{+1.25}_{-1.14}$	$0.98^{+0.53}_{-0.48}$
(5) indices, color excess	...	...	$2.31^{+1.93}_{-1.78}$	$0.39^{+0.33}_{-0.31}$

Notes. The results adopted in the paper are those obtained by simultaneously fitting three stellar absorption features, the UV flux ratio, and the observer-frame $J-H$ color (bold face). The other fits explore the effect of changing the observational constraints (see the text).

ful reading of the manuscript and stimulating discussions; and D. Bettoni for sharing his X-shooter observations of stars. We also thank the anonymous referee for very useful suggestions. We gratefully acknowledge support from the Lundbeck foundation. The Dark Cosmology Centre is funded by the Danish National Research Foundation.

APPENDIX A

STELLAR POPULATIONS: COMPARISON BETWEEN DIFFERENT OBSERVATIONAL CONSTRAINTS

As discussed in Section 4, we derive physical parameter estimates following a Bayesian approach in which we compare the observed stellar absorption features, the rest-frame UV and optical color with the predictions of a large library of stochastic SFHs. Taking advantage of the large wavelength coverage of the X-shooter spectrum, in this Appendix we explore the sensitivity of the derived parameters and associated uncertainties to the observational constraints adopted. In particular, we repeat the analysis by using either only one color (rest-frame optical or UV) in addition to the absorption indices (entries 2 and 3, respectively, in Table 6) or the pixel-by-pixel flux over the rest-frame UV and optical range (up to 5900 Å; entry 4 in Table 6). Finally, we compare with the results obtained by fitting only the absorption indices to dust-free models and estimating the dust attenuation from the difference between the observed $J-H$ color and the color of the redshifted, dust-free model spectra (thus effectively assuming a single-screen dust distribution and an attenuation law $A_\lambda \propto \lambda^{-0.7}$, and excluding models that would predict a negative dust attenuation; entry 5 in Table 6). The latter approach is similar to the one adopted in the analysis of SDSS optical spectra by Kauffmann et al. (2003) and Gallazzi et al. (2005).

In Figure 8, we show the full one- and two-dimensional probability density functions of the physical parameters of interests (i.e., marginalized over all the parameters except the ones shown in each panel) as obtained with the different observational constraints. The results are summarized in terms of medians and percentiles of the one-dimensional PDFs in Table 6. We note the following.

- The luminosity- and the mass-weighted age estimates agree well within the typical uncertainty of ∼0.1 dex, although the pixel-by-pixel fit tends to provide slightly older ages than the fits to the absorption indices alone or in combination with broadband information.
- There is a mild age–dust degeneracy in the sense that older ages are associated with lower dust attenuation. Instead, there is no clear age–metallicity degeneracy, partly because of the different sensitivity of the absorption indices to the two parameters, and partly because of the larger uncertainties in metallicity with respect to age as expected for young stellar populations (e.g., Gallazzi et al. 2005). In general degeneracies between parameters are attenuated when fitting individual absorption features rather than the full SED.
- The different slope in the A_{FUV}–A_V PDFs is a consequence of the different dust geometry assumed.
- All the fits indicate a rather large attenuation by dust, although in general fits to the rest-frame optical wavelength range tend to predict lower overall dust attenuation, and in particular underestimate the attenuation in the UV. The need to include constraints from the UV in order to correctly predict the dust attenuation is further illustrated in Figure 9 where the best-fit models to the five different sets of observational constraints are overplotted on the observed spectrum: the best fits to the optical overpredict the flux in the UV.

Overall there is good agreement among the various fits, in particular on stellar age. We note that our default fit combines the sensitivity of UV and optical colors to dust attenuation and the ability of stellar absorption features to alleviate parameter degeneracies.

APPENDIX B

FITTING X-SHOOTER TEMPLATE STELLAR SPECTRA

As an independent test of the velocity dispersion derived with pPXF, we fit stellar template spectra convolved with Gaussians to the galaxy spectrum to estimate the velocity dispersion through a chi-squared analysis (see Barth et al. 2002; Wold et al. 2007). For stellar templates we use stars of five different spectral types (AV, F5V, G8IV, K0III, K0V), observed with X-shooter at the same slit width, for a different program (084.B-035A; PI: Hjorth). In order to estimate the velocity dispersion of the

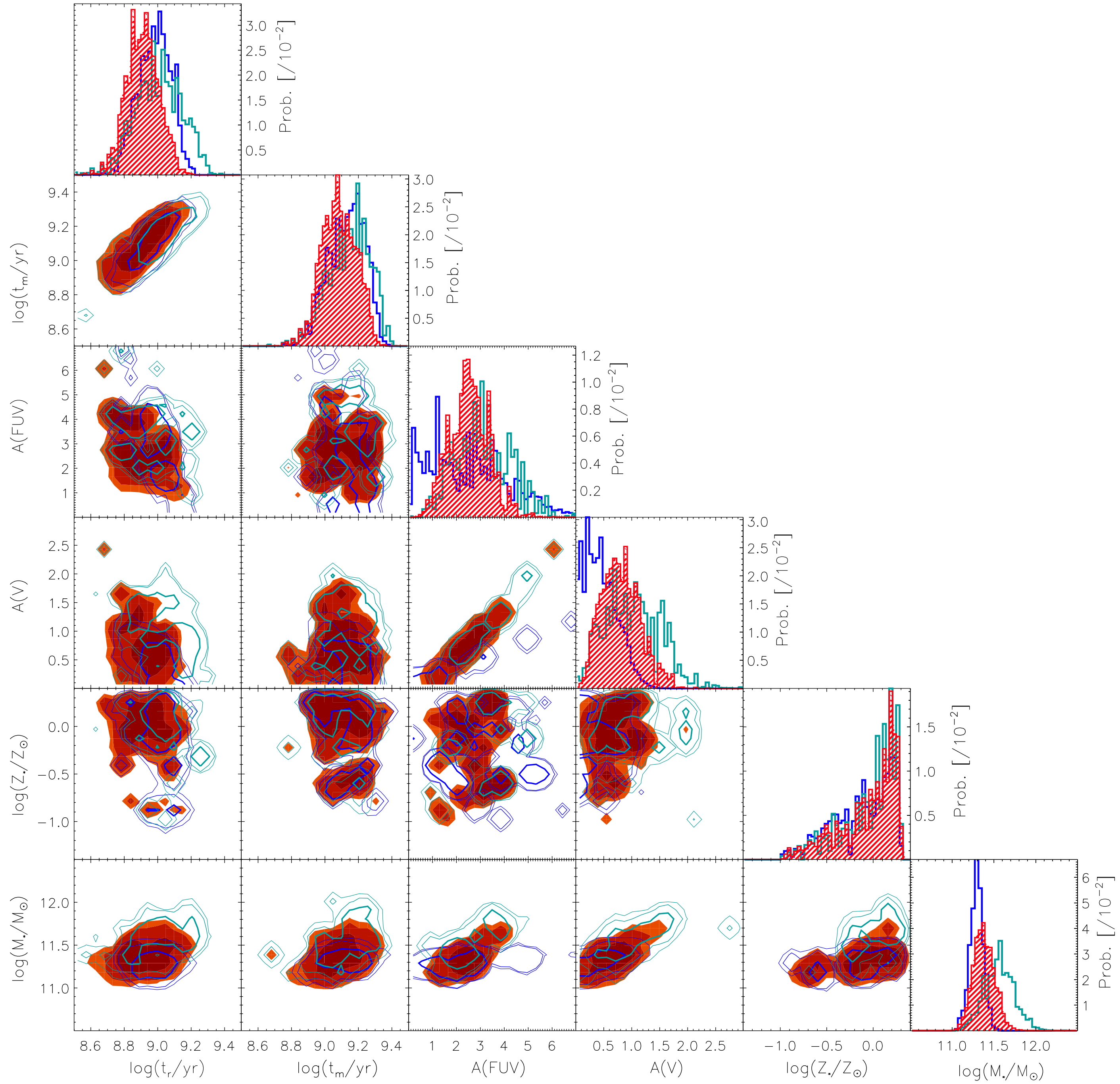

Figure 8. One- and two-dimensional marginalized probability density functions for the physical parameters estimated using different observational constraints. The filled red histograms and contours show the results of our reference fit to the absorption indices, UV, and optical colors. These are compared to the constraints obtained by fitting the absorption indices only (blue histograms and contours; Fit 5 in Table 6) or the pixel-by-pixel spectrum (green histograms and contours, Fit 4 in Table 6). The contours enclose the 68%, 85%, and 99% confidence levels. For clarity we omit the results obtained by fitting either the UV or the optical color in addition to the absorption indices, noting that they are bracketed by the PDFs shown here.

(A color version of this figure is available in the online journal.)

galaxy, we convolved these stellar spectra with Gaussians and fitted them to the Balmer line region of the galaxy spectrum.

The rest-frame wavelength range of the NIR arm in the galaxy spectrum corresponds approximately to the wavelength range of the UVB arm in the stellar spectra. When we do the spectral fitting, we therefore compare the stellar UVB to the NIR galaxy spectrum. The stellar spectra were reduced with a spectral sampling of 0.2 Å pixel^{-1} in the UVB arm and 0.5 Å pixel^{-1} in the NIR arm. The spectral sampling in the NIR arm of the galaxy spectrum corresponds to 0.16 Å pixel^{-1} in the galaxy rest frame. As this is very similar to the sampling of the UVB stellar spectra, and because of the lower quality of the galaxy spectrum compared to the stellar spectra, we chose to use the spectra as they are without further manipulation and resampling. Both the galaxy spectrum and the stellar spectra were normalized by their continua before fitting. For the stellar spectra, we extracted the continuum by marking anchor points in the spectra and doing a spline fit with varying degrees of tension. Due to the lower

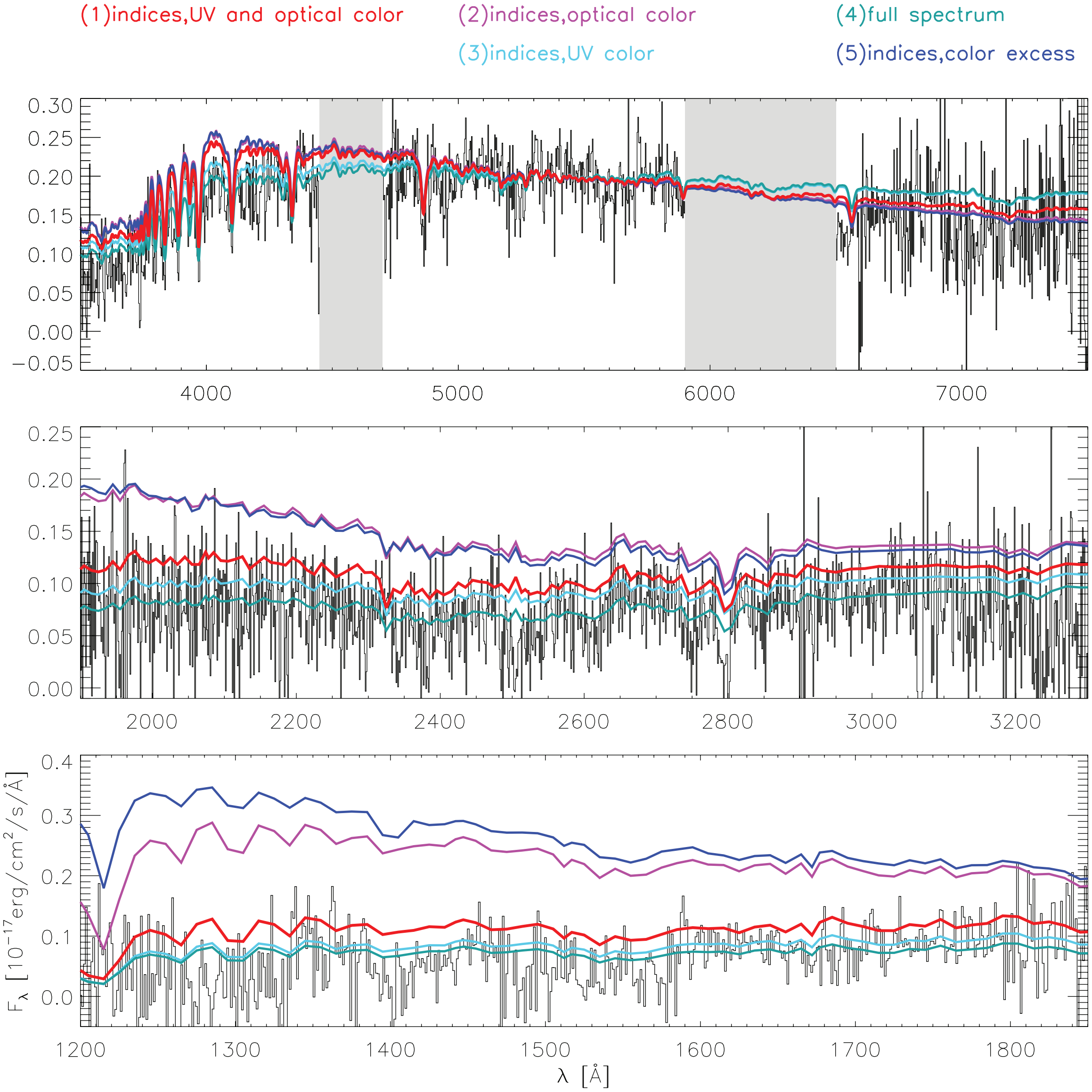

Figure 9. X-shooter spectrum at medium resolution (3 Å/bin in the NIR arm, 16 Å per bin in the UVB and VIS arms) over the full wavelength range covered by the three arms. Overplotted are the best-fit model spectra obtained by constraining (1) three stellar absorption indices, one rest-frame optical color, and the UV flux ratio (red, our default fit); (2) three stellar absorption indices and one rest-frame optical color (magenta); (3) three stellar absorption indices and the UV flux ratio (cyan); (4) the full spectrum pixel by pixel up 5900 Å (green); and (5) three stellar absorption indices and a cut on color excess (blue). Fits obtained by constraining the optical wavelength range only underpredict the dust attenuation in the UV and hence overpredict the UV flux. In the NIR spectrum, we have masked out areas of high background contamination.

(A color version of this figure is available in the online journal.)

S/N we used a different approach for the galaxy spectrum, and extracted the continuum shape from the best-fitting model of the galaxy (see Section 4) with sampling every 50 Å.

We experimented with fitting different regions of the spectrum to maximize the S/N in the velocity dispersion measurement, including as many absorption lines as possible, while down-weighting regions of the spectrum with low S/N or strong sky-line residuals. We obtained the best results by fitting the region between rest-frame wavelength 3785 Å and 5000 Å where most of the strong absorption features are found. This region covers the region blueward of Hβ. The Mg I triplet at ≈5175 Å redward of Hβ and the Na doublet (5889.95, 5895.92 Å) are not detected in the spectrum; hence we concentrated on estimating the velocity dispersion from the Balmer line region.

The AV and F5V stars (which have prominent Balmer lines) provide good fits with well constrained minima in the χ^2 distribution. The other stars provide significantly worse fits. The K0V has a minimum consistent with the best-fitting values of the K0V and F5V stars, but with a much flatter χ^2 distribution, while the G8IV and K0III do not produce a minimum, due to too weak Balmer lines and too strong *G* band and Ca H+K lines. We also fit different linear combinations of the AV and F5V stars. These fits produce consistent best-fitting values, but with slightly smaller error bars. In Figure 10 and Table 7, we show the results from the best fits. From this analysis the best-fitting velocity dispersion is in the range 260–300 km s^{-1} with a typical (random) uncertainty of 50 km s^{-1}, in agreement with the results from the pPXF fits.

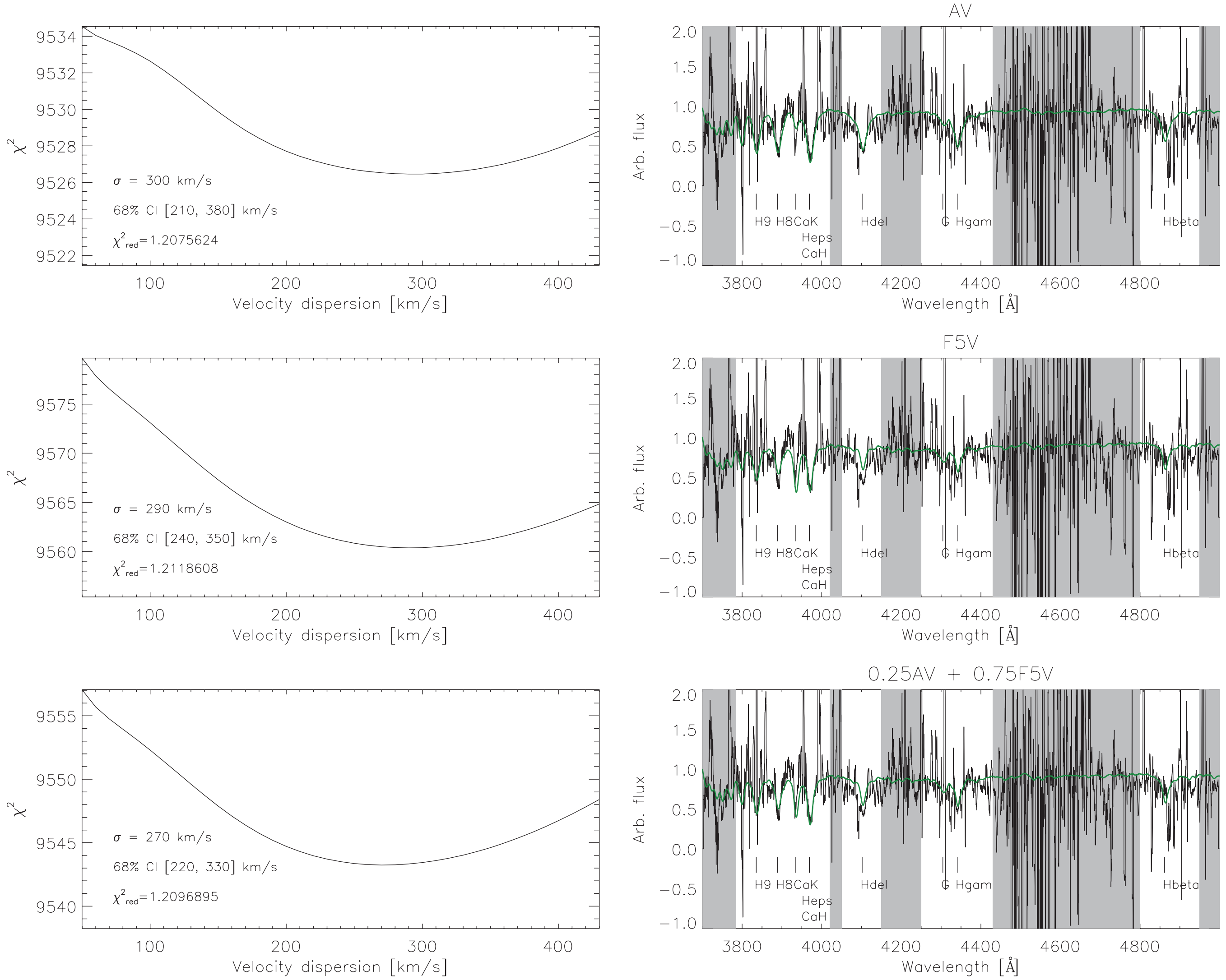

Figure 10. Fits to the galaxy spectrum with the A and F stars, and the best-fitting mixture. Regions excluded in the fit are shaded in gray. The galaxy spectrum is smoothed to a resolution of 10 Å for display purposes.

(A color version of this figure is available in the online journal.)

Table 7
Stellar Templates Used in Velocity Dispersion Fitting

Template	Spectral Type Mix (%)		σ	68% CI
	AV	F5V	(km s^{-1})	(km s^{-1})
1	100	0	300	[210,380]
2	0	100	290	[240,350]
4	75	25	270	[200,340]
5	50	50	260	[200,330]
6	25	75	270	[220,330]

Notes. The best-fit velocity dispersion and 68% confidence interval is listed in the last two columns. All fits were done in the region between 3785 and 5000 Å (rest frame) as explained in the text.

REFERENCES

Auger, M. W., Treu, T., Bolton, A. S., et al. 2010, ApJ, 724, 511

Barth, A. J., Ho, L. C., & Sargent, W. L. W. 2002, AJ, 124, 2607

Bezanson, R., van Dokkum, P. G., Tal, T., et al. 2009, ApJ, 697, 1290

Blain, A. W., Jameson, A., Smail, I., et al. 1999, MNRAS, 309, 715

Blanton, M. R., Schlegel, D. J., Strauss, M. A., et al. 2005, AJ, 129, 2562

Bohlin, R. C. 2007, in ASP Conf. Ser. 364, The Future of Photometric, Spectrophotometric and Polarimetric Standardization, ed. C. Sterken (San Francisco, CA: ASP), 315

Bohlin, R. C., & Gilliland, R. L. 2004, AJ, 128, 3053

Bolton, A. S., Burles, S., Koopmans, L. V. E., Treu, T., & Moustakas, L. A. 2006, ApJ, 638, 703

Boylan-Kolchin, M., Ma, C.-P., & Quataert, E. 2005, MNRAS, 362, 184

Bruzual, G., & Charlot, S. 2003, MNRAS, 344, 1000

Cameron, E., Carollo, C. M., Oesch, P. A., et al. 2011, ApJ, 743, 146

Capak, P., Carilli, C. L., Lee, N., et al. 2008, ApJ, 681, L53

Cappellari, M., Bacon, R., Bureau, M., et al. 2006, MNRAS, 366, 1126

Cappellari, M., di Serego Alighieri, S., Cimatti, A., et al. 2009, ApJ, 704, L34

Cappellari, M., & Emsellem, E. 2004, PASP, 116, 138

Carignan, C., & Beaulieu, S. 1989, ApJ, 347, 760

Cassata, P., Giavalisco, M., Guo, Y., et al. 2011, ApJ, 743, 96

Cenarro, A. J., & Trujillo, I. 2009, ApJ, 696, L43
Chabrier, G. 2003, PASP, 115, 763
Charlot, S., & Fall, S. M. 2000, ApJ, 539, 718
Cimatti, A., Cassata, P., Pozzetti, L., et al. 2008, A&A, 482, 21
Cimatti, A., Nipoti, C., & Cassata, P. 2012, MNRAS, 422, L62
Conselice, C. J., Bluck, A. F. L., Buitrago, F., et al. 2011, MNRAS, 413, 80
Daddi, E., Renzini, A., Pirzkal, N., et al. 2005, ApJ, 626, 680
Daddi, E., Röttgering, H. J. A., Labb, I., et al. 2003, ApJ, 588, 50
Damjanov, I., Abraham, R. G., Glazebrook, K., et al. 2011, ApJ, 739, L144
di Serego Alighieri, S., Vernet, J., Cimatti, A., et al. 2005, A&A, 442, 125
Falcón-Barroso, J., Sánchez-Blázquez, P., Vazdekis, A., et al. 2011, A&A, 532, A95
Ferré-Mateu, A., Vazdekis, A., Trujillo, I., et al. 2012, MNRAS, 423, 632
Ferreras, I., Saha, P., & Williams, L. L. R. 2005, ApJ, 623, L5
Franx, M., Labbé, I., Rudnick, G., et al. 2003, ApJ, 587, L79
Franx, M., van Dokkum, P. G., Schreiber, N. M. F., et al. 2008, ApJ, 688, 770
Gallazzi, A., Brinchmann, J., Charlot, S., & White, S. D. M. 2008, MNRAS, 383, 1439
Gallazzi, A., Charlot, S., Brinchmann, J., & White, S. D. M. 2006, MNRAS, 370, 1106
Gallazzi, A., Charlot, S., Brinchmann, J., White, S. D. M., & Tremonti, C. A. 2005, MNRAS, 362, 41
Gawiser, E., van Dokkum, P. G., Herrera, D., et al. 2006, ApJS, 162, 1
Goto, T. 2005, MNRAS, 357, 937
Greve, T. R., Bertoldi, F., Smail, I., et al. 2005, MNRAS, 359, 1165
Grillo, C. 2010, ApJ, 722, 779
Grillo, C., Gobat, R., Lombardi, M., & Rosati, P. 2009, A&A, 501, 461
Hopkins, P. F., Hernquist, L., Cox, T. J., Robertson, B., & Springel, V. 2006, ApJS, 163, 50
Horne, K. 1986, PASP, 98, 609
Jørgensen, I., Franx, M., & Kjaergaard, P. 1996, MNRAS, 280, 167
Kelson, D. D., Illingworth, G. D., van Dokkum, P. G., & Franx, M. 2000, ApJ, 531, 184
Kauffmann, G., Heckman, T. M., White, S. D. M., et al. 2003, MNRAS, 341, 33
Kennicutt, R. C., Jr. 1998, ARA&A, 36, 189
Khochfar, S., & Silk, J. 2006, ApJ, 648, L21
Kriek, M., van Dokkum, P. G., Franx, M., et al. 2006, ApJ, 649, L71
Kriek, M., van Dokkum, P. G., Labbé, I., et al. 2009, ApJ, 700, 221
Lucey, J. R., Bower, R. G., & Ellis, R. S. 1991, MNRAS, 249, 755
Man, A. W. S., Toft, S., Zirm, A. W., Wuyts, S., & van der Wel, A. 2012, ApJ, 744, 85
Mancini, C., Daddi, E., Renzini, A., et al. 2010, MNRAS, 401, 933
Marchesini, D., van Dokkum, P., Quadri, R., et al. 2007, ApJ, 656, 42
Marchesini, D., van Dokkum, P. G., Förster Schreiber, N. M., et al. 2009, ApJ, 701, 1765
Martinez-Manso, J., Guzman, R., Barro, G., et al. 2011, ApJ, 738, L22
McCracken, H. J., Capak, P., Salvato, M., et al. 2010, ApJ, 708, 202
McCracken, H. J., Milvang-Jensen, B., Dunlop, J., et al. 2012, arXiv:1204.6586
Michałowski, M. J., Dunlop, J. S., Cirasuolo, M., et al. 2012, A&A, 541, A85
Naab, T., Johansson, P. H., & Ostriker, J. P. 2009, ApJ, 699, L178
Naab, T., Johansson, P. H., Ostriker, J. P., & Efstathiou, G. 2007, ApJ, 658, 710
Newman, A. B., Ellis, R. S., Bundy, K., & Treu, T. 2011, ApJ, 746, 162
Newman, A. B., Ellis, R. S., Treu, T., & Bundy, K. 2010, ApJ, 717, L103
Oke, J. B. 1974, ApJS, 27, 21
Onodera, M., Daddi, E., Gobat, R., et al. 2010, ApJ, 715, L6
Oser, L., Naab, T., Ostriker, J. P., & Johansson, P. H. 2012, ApJ, 744, 63
Padmanabhan, N., Seljak, U., Strauss, M. A., et al. 2004, New Astron., 9, 329
Peng, C. Y., Ho, L. C., Impey, C. D., & Rix, H.-W. 2002, AJ, 124, 266
Persic, M., Salucci, P., & Stel, F. 1996, MNRAS, 281, 27
Quadri, R. F., Williams, R. J., Lee, K.-S., et al. 2008, ApJ, 685, L1
Quintero, A. D., Hogg, D. W., Blanton, M. R., et al. 2004, ApJ, 602, 190
Rettura, A., Rosati, P., Strazzullo, V., et al. 2006, A&A, 458, 717
Salim, S., Charlot, S., Rich, R. M., et al. 2005, ApJ, 619, L39
Sánchez-Blázquez, P., Peletier, R. F., Jiménez-Vicente, J., et al. 2006, MNRAS, 371, 703
Schlegel, D. J., Finkbeiner, D. P., & Davis, M. 1998, ApJ, 500, 525
Sérsic, J. L. 1968, Atlas de Galaxias Australes (Cordoba, Argentina: Observatorio Astronomico)
Shankar, F., Marulli, F., Bernardi, M., et al. 2011, arXiv:1105.6043
Shih, H.-Y., & Stockton, A. 2011, ApJ, 733, 45
Sonnenfeld, A., Treu, T., Gavazzi, R., et al. 2011, arXiv:1111.4215
Strigari, L. E., Frenk, C. S., & White, S. D. M. 2010, MNRAS, 408, 2364
Szomoru, D., Franx, M., & van Dokkum, P. G. 2011, ApJ, 749, 121
Szomoru, D., Franx, M., van Dokkum, P. G., et al. 2010, ApJ, 714, L244
Tacconi, L. J., Genzel, R., Smail, I., et al. 2008, ApJ, 680, 246
Tacconi, L. J., Neri, R., Chapman, S. C., et al. 2006, ApJ, 640, 228
Taylor, E. N., Franx, M., Glazebrook, K., et al. 2010, ApJ, 720, 723
Thomas, D., Maraston, C., & Bender, R. 2003, MNRAS, 339, 897
Toft, S., Franx, M., van Dokkum, P., et al. 2009, ApJ, 705, 255
Toft, S., van Dokkum, P., Franx, M., et al. 2005, ApJ, 624, L9
Toft, S., van Dokkum, P., Franx, M., et al. 2007, ApJ, 671, 285
Treu, T., Auger, M. W., Koopmans, L. V. E., et al. 2010, ApJ, 709, 1195
Tremonti, C. A., Heckman, T. M., Kauffmann, G., et al. 2004, ApJ, 613, 898
Trujillo, I., Cenarro, A. J., de Lorenzo-Cáceres, A., et al. 2009, ApJ, 692, L118
Trujillo, I., Förster Schreiber, N. M., Rudnick, G., et al. 2006, ApJ, 650, 18
Tumlinson, J. 2007, ApJ, 665, 1361
van de Sande, J., Kriek, M., Franx, M., et al. 2011, ApJ, 736, L9
van der Wel, A., Franx, M., van Dokkum, P. G., & Rix, H.-W. 2004, ApJ, 601, L5
van der Wel, A., Rix, H.-W., Wuyts, S., et al. 2011, ApJ, 730, 38
van Dokkum, P. G. 2008, ApJ, 674, 29
van Dokkum, P. G., & Franx, M. 1996, MNRAS, 281, 985
van Dokkum, P. G., Franx, M., Kriek, M., et al. 2008, ApJ, 677, L5
van Dokkum, P. G., Kriek, M., & Franx, M. 2009, Nature, 460, 717
van Dokkum, P. G., Quadri, R., Marchesini, D., et al. 2006, ApJ, 638, L59
van Dokkum, P. G., & van der Marel, R. P. 2007, ApJ, 655, 30
van Dokkum, P. G., Whitaker, K. E., Brammer, G., et al. 2010, ApJ, 709, 1018
Vernet, J., Dekker, H., D'Odorico, S., et al. 2011, A&A, 536, A105
Wilkins, S. M., Hopkins, A. M., Trentham, N., & Tojeiro, R. 2008, MNRAS, 391, 363
Williams, R. J., Quadri, R. F., Franx, M., et al. 2010, ApJ, 713, 738
Wold, M., Lacy, M., & Armus, L. 2007, A&A, 470, 531
Worthey, G. 1994, ApJS, 95, 107
Wuyts, S., Cox, T. J., Hayward, C. C., et al. 2010, ApJ, 722, 1666
Wuyts, S., Förster Schreiber, N. M., van der Wel, A., et al. 2011, ApJ, 742, 96
Yang, Y., Zabludoff, A. I., Zaritsky, D., Lauer, T. R., & Mihos, J. C. 2004, ApJ, 607, 258
Zirm, A. W., van der Wel, A., Franx, M., et al. 2007, ApJ, 656, 66
Zirm, A. W., Toft, S., & Tanaka, M. 2012, ApJ, 744, 181